Received: 25 May 2022 | Revised: 26 July 2022 | Accepted: 10 August 2022

DOI: 10.1002/agt2.266

Aggregate WILEY

REVIEW

Atomically precise copper nanoclusters as ultrasmall molecular aggregates: Appealing compositions, structures, properties, and applications

Leon Li-Min Zhang[1,2] | **Wai-Yeung Wong**[1,2]

[1]Department of Applied Biology and Chemical Technology and Research Institute for Smart Energy, The Hong Kong Polytechnic University, Hong Kong, P. R. China

[2]Shenzhen Research Institute, The Hong Kong Polytechnic University, Shenzhen, P. R. China

Correspondence
Wai-Yeung Wong, Department of Applied Biology and Chemical Technology and Research Institute for Smart Energy, The Hong Kong Polytechnic University, Hong Kong Special Administrative Region, P. R. China.
Email: wai-yeung.wong@polyu.edu.hk

Funding information
Science, Technology and Innovation Committee of Shenzhen Municipality, Grant/Award Number: JCYJ20180507183413211; RGC Senior Research Fellowship Scheme, Grant/Award Number: SRFS2021-5S01; Hong Kong Research Grants Council, Grant/Award Number: PolyU153062/18P; Guangdong-Hong Kong-Macao Joint Laboratory of Optoelectronic and Magnetic Functional Materials, Grant/Award Number: 2019B121205002; Hong Kong Polytechnic University, Grant/Award Number: 1-ZE1C; Research Institute for Smart Energy, Grant/Award Number: CDAQ; Miss Clarea Au for the Endowed Professorship in Energy, Grant/Award Number: 847S

Abstract

Metal nanoclusters (NCs) are ultrasmall molecular aggregates consisting of dozens to hundreds of metal atoms consolidated by organic ligands, which represent an emerging area of nanoscience. Amide a myriad of metal NCs, copper NCs (CuNCs) comprise a low-cost, high-value subclass that has attracted great attention. The variable copper cores and diversity of protecting ligands have rendered CuNCs interesting molecular aggregates featuring structural and compositional versatility, hence showing distinctive properties and potential applications. In the present review, we have summarized the progress on atomically precise CuNCs that exhibit a range of appealing properties and applications in different fields. This review is expected to provide not only an overview of the current development on atomically precise CuNCs, but also possible directions for the future design of novel CuNCs for fundamental studies and practical applications.

KEYWORDS

applications, atomically precise structures, copper nanoclusters, properties

1 | INTRODUCTION

Atomically precise metal nanoclusters (NCs) are discrete molecular aggregates composed of several to a few hundreds of metal atoms passivated by organic ligands, which have attracted great attention in chemical science and materials science fields.[1] As an appealing class of aggregates, metal NCs have a size of 1 to 3 nm, which falls between the single atoms (non-aggregated) and nanoparticles (aggregated, >3 nm) to bestow an intriguing size effect.[2] On the one hand, such ultrasmall size is close to the Fermi wavelength of electrons, which leads to the breakup of continuous energy levels into discrete levels.[3] As a result, the quantum confinement effect has imparted metal NCs with molecule-like materials properties, and consequently persistent efforts have been paid to delve into the experimental realms of these properties and relevant applications.[4] On the other hand, this size regime is well within the resolving limit of single-crystal X-ray diffraction, which allows chemists to understand their nanostructures at an atomic precision. Under this background, atomically precise metal NCs are expected to emerge as promising materials to exhibit fascinating nanostructures and properties, which is highly important for both fundamental scientific studies and practical applications.[5]

Compared with NCs based on the noble metals of platinum (Pt), gold (Au), and silver (Ag), those based on copper (Cu) have attracted peculiar interest on account of the high earth abundance, low cost, and low toxicity of Cu.[6] Undoubtedly, the composition and structure of CuNCs play an essential role to evoke their intriguing properties. First, the nuclearity and arrangement of Cu atoms can directly determine the Cu core structures. Second, the various oxidation states of Cu

including +II, +I, and 0 can naturally nourish diverse Cu cores. In this respect, benefiting from the development of synthetic methodologies, CuNCs bearing Cu(0), superatom (oxidation state between 0 and I), homo-valent Cu(I), and mixed-valent Cu(I)/Cu(II) characters have been prepared.[7] Third, the outermost organic ligands can not only protect the Cu cores from aggregation to form metallo-polymers, but also facilitate the formation of novel CuNCs. Thus, ligands including thiolate, alkynyl, phosphine, and selenol have been utilized to engender a diversity of CuNCs.[8] Last but not least, hydrides (H^-) have also been introduced to generate Cu hydride NCs as an appealing class of CuNCs.[9] Thanks to such remarkable flexibility on compositions and structures, CuNCs have been revealed to exhibit inherently variable properties and applications.

Liu and Astruc, Nakajima, Sun, and Tanase et al. have successively reviewed the progress on Cu(I) hydride NCs.[6,10–12] Bürgi et al. have highlighted some functional CuNCs.[13] Recently, Wang and Rogach et al. have reviewed the aggregation-induced emission (AIE) active CuNCs.[14] Herein, we attempt to summarize CuNCs featuring well-defined compositions and structures to show intriguing properties and applications. In this review, CuNCs with atomically precise compositions and structures (TABLE 1) will be classified by their properties and applications. First, CuNCs with intriguing photophysical properties including near-infrared (NIR) emissions, AIE, and/or circularly polarized luminescence (CPL) are presented. Then, CuNCs with functional applications in CO_2 electrochemical reduction (CO_2 ERR), chemical sensing, catalysis in organic synthesis, and electronic devices are described. Finally, we have suggested some current challenges and prospects that may deserve in-depth research for future endeavors.

2 | PHOTOPHYSICAL PROPERTIES OF CuNCs

Photophysical properties constitute one of the most exciting properties of CuNCs.[15,16] Generally, the photoluminescence mechanism of CuNCs is controlled by metal-ligand interface chemistry. While CuNCs exhibit a diversity of compositions and structures with different Cu cores and protecting ligands, their photoluminescence manifests in variable emission behaviors, which are quite specific to the exact CuNCs. The merits of the photophysical properties of CuNCs usually include good photostability, large Stokes shift, wide emission wavelength range, and long emission lifetime.[17] Based on the variable photophysical properties, a group of emission behaviors including NIR emission, AIE, and CPL has been revealed.

2.1 | NIR emission

NIR emitting materials have been long-sought in the fields of chemistry, biomedical and materials science, which is due to their advantages including less scattering, deep penetration, and low light absorption.[18] It has been reported that the presence of cuprophilic Cu(I)···Cu(I) interactions, which occur between two closed-shell d^{10} Cu(I) cations with their distance less than the sum of their van der Waals radius (1.4 Å × 2), is conducive to evoke the NIR emissions.[17] In practice, it is still a challenging task to predict the structures of NIR-emitting CuNCs, as compared to the well-established situation for the design of AuNCs as NIR emitters. So far, only a handful of CuNCs have been revealed to show NIR emissions with the emission wavelength longer than 700 nm.

Fenske et al. have pioneered the works on emissive Cu chalcogenide NCs, wherein they have devoted to synthesizing and characterizing a diversity of CuNCs with nuclearity ranging from several to more than a hundred.[19] Established on their extensive studies, they have reported two intriguing NCs, $[Cu_{26}Se_{13}(PEt_2Ph)_{14}]$ (**CuNC-1**) and $[Cu(I)_{44}Se_{22}(PEt_2Ph)_{18}]$ (**CuNC-2**). As shown in Figure 1A-a, the cluster framework of **CuNC-1** can be described as a packing of Cu and Se polyhedra: the central Se1 atom is surrounded by a slightly distorted Cu_{12} icosahedron. In turn, a Se_{12} icosahedron is situated around the $SeCu_{12}$ core. Finally, a six-fold capped cube of the Cu atoms binds to fourteen PEt_2Ph ligands to furnish **CuNC-1**. In contrast, **CuNC-2** contains a Se_{20} deltohedron with two additional Se atoms (Se8 and Se15) located at the center. Of the forty-four copper atoms, eighteen are situated above and eighteen below the triangles of the Se_{12}. The chalcogen polyhedron is shielded by eighteen PEt_2Ph ligands with an almost closed ligand shell (Figure 1A-b). **CuNC-1** and **CuNC-2** both show weak NIR emissions at room temperature (Figure 1A-c). Their emission intensities increase by decreasing the temperature to 16 K, and as the nuclearity increases, the emission maximum grows and extends to the second NIR window (1000 to 1700 nm) at 16 K, from 835 nm through 1010 to 1120 nm. It should be highlighted that NCs emitting light in the second near-infrared (NIR-II) window are rare, as compared to materials with emissions in the visible and first infrared region (700 to 1000 nm).

Eichhöfer et al. have designed a series of phosphine-stabilized Cu(I) chalcogenide NCs to reveal that the Cu(I) cores, as well as the phosphine ligands distinguish these NCs from each other in terms of their emission property.[20] Of particular interest are $[Cu(I)_{20}S_{10}(PPh_3)_8]$ (**CuNC-3**) and $[Cu(I)_{20}S_{10}(P^tBu_3)_8]$ (**CuNC-4**), as shown in Figure 1B-a,b, which are the oblate and prolate isomers of a cluster composition $[Cu_{20}S_{10}(PR_3)_8]$, respectively. The cluster core of **CuNC-3** can be considered as a dimer of two fused '$Cu_{12}S_6$' cages fused from the top/bottom of the cluster. In this way, ten sulfur atoms form a bicapped tetragonal prism with the Cu atoms bridging all edges. The cluster core of **CuNC-4** has no direct relation to the $Cu_{12}S_6$ cluster core. It can be taken as a S_{10} polyhedron of a highly compressed tetragonal antiprism bridged by Cu atoms, coordinated by two sulfur atoms and twelve copper atoms, which are further stabilized by two sulfur atoms and one phosphorus atom. As shown in Figure 1B-c, **CuNC-3** shows a broad emission that is centered at 823 nm and extends to 1200 nm, and **CuNC-4** displays a relatively weak orange emission at 575 nm, which shifts to 587 and 795 nm at 20 K. These results demonstrate that the NIR emissions of Cu chalcogenide NCs can be affected by the kind of phosphine ligands and NC geometry.

Latouche, Liu, and Saillard et al. have explored the emission property of $[Cu_{11}(\mu_9\text{-I})(\mu_3\text{-I})_3(Se_2P(OH)_2)_6]$ (**CuNC-5**).[21] As shown in Figure 2A-a,b, **CuNC-5** has a penta-capped trigonal prismatic $Cu_{11}(\mu_9\text{-I})$ core. The cluster cation has an idealized C_{3h} symmetry, and two kinds of iodide ion

TABLE 1 Summary of reported atomically precise CuNCs

CuNCs	Formulas	Ref.
CuNC-1	$[Cu_{26}Se_{13}(PEt_2Ph)_{14}]$	[19]
CuNC-2	$[Cu(I)_{44}Se_{22}(PEt_2Ph)_{18}]$	[19]
CuNC-3	$[Cu(I)_{20}S_{10}(PPh_3)_8]$	[20]
CuNC-4	$[Cu(I)_{20}S_{10}(P^tBu_3)_8]$	[20]
CuNC-5	$[Cu_{11}(\mu_9\text{-I})(\mu_3\text{-I})_3(Se_2P(OH)_2)_6]$	[21]
CuNC-6	$[Cu(I)_{13}(SePh)_{13}(Ph_3P)_4]$	[22]
CuNC-7	$[Cu(I)_{11}(TBBT)_9(PPh_3)_6](SbF_6)_2$[a]	[23]
CuNC-8	$[^tBuC{\equiv}CCu(I)]_{20}{\cdot}C_6H_6$	[24]
CuNC-9	$[Cu(I)_{15}(^tBuC{\equiv}C)_{10}(CF_3COO)_5]{\cdot}{}^tBuC{\equiv}CH$	[25]
CuNC-10	$[Cu(I)_{15}(^tBuC{\equiv}C)_{14}NO_3]$	[26]
CuNC-11	$[Cu(I)_{28}(^tBuC{\equiv}C)_{22}(SO_4)_2(OMe)_2]$	[26]
CuNC-12-R/S	$[Cu(I)_{14}(R/S\text{-DPM})_8](PF_6)_6$[b]	[31]
CuNC-13-D/L	[D/L-valinol(18-crown-6)][$Cu(I)_5(S^tBu)_6$]	[32]
CuNC-14-R/S	$[Cu(I)_3(R/S\text{-BINAP})_3CO_3](^tBuSO_3)$[c]	[33]
CuNC-15	$[Cu(I)_{15}(PPh_3)_6(PET)_{13}](BF_4)_2$[d]	[34]
CuNC-16	$[Cu(I)_8(^tBuC_6H_4S)_8(PPh_3)_4]$	[35]
CuNC-17	$[Cu(0)_4Cu(I)_{10}DT_{10}]$[e]	[36, 37]
CuNC-18	$[Cu(I)_{14}H_{12}(phen)_6(PPh_3)_4][Cl]_2$[f]	[43]
CuNC-19	$[Cu(I)_{32}H_{20}\{S_2P(OiPr)_2\}_{12}]$	[44]
CuNC-20	$[Cu(I)_{25}H_{22}(PH_3)_{12}]Cl$	[48]
CuNC-21	$[Cu_{13}(MBO)_{12}H]$[g]	[49]
CuNC-22	$[Cu_6(SC_7H_4NO)_6][Na(C_3H_6O)_6]$	[53]
CuNC-23	$[Cu_{14}(C_2B_{10}H_{10}S_2)_6(CH_3CN)_8]$	[55]
CuNC-24	$[Cu(I)_8(\mu_4\text{-H})\{S_2P(OEt)_2\}_6][PF_6]$	[57]
CuNC-25	$[Cu_{20}(C{\equiv}CPh)_{12}(OAc)_6)]$	[58]
CuNC-26	$[Cu(I)_{25}H_{10}(SPhCl_2)_{18}](PPh_4)_3$	[60]
CuNC-27	$[Cu(I)_8H_6(\mu\text{-dpmppm})_3](PF_6)_2$[h]	[61]
CuNC-28	$[Cu(I)_8H_6(\mu\text{-dppm})_5](PF_6)_2$[i]	[62]
CuNC-29	$[Cu_{53}(4\text{-FC}{\equiv}CPh)_9(dppp)_6Cl_6(OAc)_6]$[j]	[63]
CuNC-30	$[Cu(I)_5(DPFN)_2H_2](NTf_2)_3$[k]	[66]
CuNC-31	$[Cu(I)_{32}(PET)_{24}H_8Cl_2](PPh_4)_2$[d]	[67]
CuNC-32a	$[Cu(I)_{13}Na_2(CZ\text{-}PrA)_6(TC4A)_2Cl(MeOH)_2]$[l]	[68]
CuNC-32b	$[Cu(I)_{13}Na(CZ\text{-}PrA)_6(TC4A)_2(MeOH)]{\cdot}MeOH{\cdot}DCM{\cdot}CH_3COCH_3$[l]	[68]
CuNC-33	$[Cu_{53}(CF_3COO)_{10}(C{\equiv}C^tBu)_{20}Cl_2H_{18}]^+$	[69]
CuNC-34	$\{[Cu(II)O_4]{\cdot}[VO_4]_2@Cu(I)_{46}(C{\equiv}C^tBu)_{27}(^tBuPO_3)_2(H_2O)\}{\cdot}(BF_4)_3$	[26]
CuNC-35	$\{[Cu(II)O_6]@Cu(I)_{47}(C{\equiv}CiPr)_{33}\}{\cdot}(ClO_4)_4$	[26]
CuNC-36	$[Cu_{23}(^tBuC{\equiv}C)_{13}(CF_3COO)_6]$	[70]

[a]TBBT = 4-*tert*-butylbenzenethiol.
[b]DPM = 2-diphenyl-2-hydroxylmethylpyrrolidine-1-propyne.
[c]BINAP = 2,2-*bis*(diphenylphosphino)-1,1-binaphthyl.
[d]PET = 2-phenylethanethiolate.
[e]DT = 1-dodecanethiol.
[f]phen = 1,10-phenanthroline.
[g]MBO = 2-mercaptobenzoxazole.
[h]dpmppm = meso-*bis*[(diphenylphosphinomethyl)phenylphosphino]methane.
[i]dppm = *bis*(diphenylphosphino)methane.
[j]dppp = 1,3-*bis*(diphenylphosphino)propane.
[k]DPFN = 2,7-*bis*(fluoro-di(2-pyr-idyl)methyl)-1,8-naphthyridine, NTf = *bis*(trifluoromethanesulfonyl)imide.
[l]CZ-PrAH = 9-(prop-2-yn-1-yl)-9H-carbazole, H_4TC4A = p-*tert*-butylthiacalix[4]arene.

(μ_9 and μ_3) can be found, and one located at the cluster center and the other situated on the peripheral of the cluster. At 77 K, a structureless emission centered at 766 nm was observed, and the emission slightly shifted to 745 nm in methylene chloride glass (Figure 2A-c). The emission origin has been assigned to the mixing of ^{3}LMCT and ^{3}LLCT. Gratifyingly, theoretical simulated emission by time-dependent (TD) density functional theory (DFT) calculation fits well with the experimental spectrum after the correction of energy shift from the limited accuracy of electronic

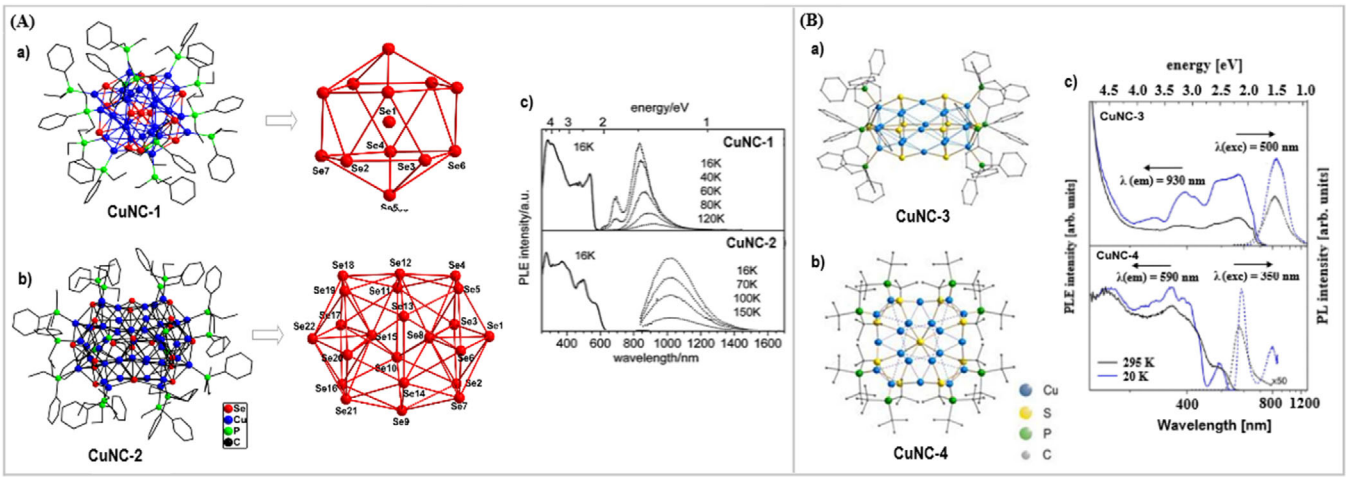

FIGURE 1 A: Structure of (a) **CuNC-1** featuring Se_{12} icosahedron and (b) **CuNC-2** featuring a Se_{20} deltohedron, and their (c) temperature-dependent emission spectra. Reproduced with permission.[19] Copyright 2013, The Royal Society of Chemistry. B: Structure of (a) **CuNC-3** and (b) **CuNC-4**, and (c) their emission spectra at 20 and 295 K. Reproduced with permission.[20] Copyright 2015, American Chemical Society

TD-DFT transitions. On this ground, these authors have also predicted that the hypothetical Cu^--incorporating NC $[Cu_{11}(\mu_9\text{-}Cu)(\mu_3\text{-}I)_3(E_2P(OH)_2)_6]^+$ (E = S, Se) shows the NIR emissions at 763 nm (E = S) and 872 nm (E = Se).

Zhu et al. have reported the cluster $[Cu(I)_{13}(SePh)_{13}(Ph_3P)_4]$ (**CuNC-6**), which exhibits a quasi-T2 construction (Figure 2B-a).[22] The $PhSe^-$ ligands in **CuNC-6** have diverse coordination modes (Figure 2B-c): (i) μ_2-Se—Cu_2, (ii) μ_3-Se—Cu_3, (iii) μ_4-Se—Cu_4 and (iv) μ_6-Se—Cu_6. The Ph_3P ligands also coordinate with the Cu atoms at four terminal vertices, and the top and side view of the $Cu_{13}Se_{13}P_4$ structure is displayed in Figure 2B-b. The thermochromic emission behavior of **CuNC-6** was revealed. As the temperature decreases, the emission wavelength blue-shifts from 727 nm at room temperature to 680 nm at 80 K (Figure 2B-d). More recently, they were also committed to report $[Cu(I)_{11}(TBBT)_9(PPh_3)_6](SbF_6)_2$ (**CuNC-7**, TBBT = 4-*tert*-butylbenzenethiol) as a red-light emitter with an absolute quantum yield of 0.22.[23] The framework of $Cu(I)_{11}$ is displayed in Figure 2C-a,b, which can be considered as a triangular bipyramid Cu_5 unit covered with three $Cu_2S_3P_2$ motifs (Figure 2C-c). In contrast, upon decreasing the temperature, the emission red-shifted from 675 nm at ambient temperature to 700 nm at 70 K (Figure 2C-d). This can be attributed to the ^{3}CC emission caused by the temperature-dependent cuprophilic Cu(I)···Cu(I) interactions.

Che et al. have conducted the seminal works on the photophysical behaviors of Cu(I) alkynyl NCs. In 2005, they reported $[^tBuC{\equiv}CCu(I)]_{20}{\cdot}C_6H_6$ (**CuNC-8**), which represents a rare example of a homoleptic $Cu(I)_{20}$ cluster with an unprecedented copper(I) ring catenation.[24] The architecture can be viewed as an interlocking of a distorted Cu_8 ring with two puckered hexagonal Cu_6 rings (Figure 3A-a,b), which is consolidated by twenty $^tBuC{\equiv}C^-$ ligands in various coordination modes of μ_2, μ_3, and μ_4. Excitation of **CuNC-8** gave a red emission peaking at 720 nm at 298 K, and at 77 K, this band can be resolved into three peaks with maxima at 620, 700, and 825 nm. This is possibly due to the structural distortion of NC or phase transition at low temperature. Such emissions are ascribed to originate from alkynyl to the Cu(I) LMCT mixed with cuprophilic interactions.

In another example, Sun et al. have reported the photophysical property of $[Cu(I)_{15}(^tBuC{\equiv}C)_{10}(CF_3COO)_5]{\cdot}{}^tBuC{\equiv}CH$ (**CuNC-9**).[25] The $Cu(I)_{15}$ cluster can be seen as a pentagonal bipyramid and two Cu_4 folding lines locked its four adjacent edges (Figure 3B-a). Furthermore, it is protected by ten $^tBuC{\equiv}C^-$ with three different bonding modes of μ_2, μ_3, and μ_4 and five μ_2-η^1:η^1 CF_3COO^- ligands (Figure 3B-b). Thermochromic luminescence was observed in the NIR region (Figure 3B-c). The emission maximum of **CuNC-9** red-shifted from 710 nm at 298 K to 793 nm at 93 K, along with a 17-fold enhancement of the emission intensity. The increased emission intensity upon cooling could be ascribed to an inhibition of the nonradiative decay at lower temperature. DFT calculations have suggested that the emission originates from the mixed ^{3}LMCT and ^{3}CC excited states, which have been impacted by the temperature-sensitive Cu(I)···Cu(I) interactions. Specifically, with lowering the temperature, Cu···Cu contacts were reduced to decrease the energy gap of the transition state to give red-shifted phosphorescence. As shown in Figure 3B-d, the volume of unit cell drops, emission intensity, and emission maxima wavelength increase with the lowering of temperature.

Later on, another study was conducted by Mak et al. to explore the photophysical property of $[Cu(I)_{15}(^tBuC{\equiv}C)_{14}NO_3]$ (**CuNC-10**) and $[Cu(I)_{28}(^tBuC{\equiv}C)_{22}(SO_4)_2(OMe)_2]$ (**CuNC-11**), which were found to display thermally activated delayed fluorescence (TADF) in the NIR region.[26] **CuNC-10** is stabilized by fourteen $^tBuC{\equiv}C^-$ ligands and one μ-κO:κO′ NO_3^- with Cu(I)—O bond lengths of 2.169 and 2.379 Å (Figure 3C-a). For **CuNC-11**, in addition to twenty-two alkynyl ligands, two μ_3-MeO^- and two μ_3-κO:κO′:κO′′ SO_4^{2-} ligands cap the respective central and terminal section of its $Cu(I)_{28}$ core to give **CuNC-11** as an elongated nanorod (Figure 3C-c). Impressively, at 77 K, **CuNC-15** displays a broad NIR emission band centered at 871 nm. Upon increasing the temperature, a continuous bathochromic effect occurred to afford an emission maximum at 731 nm at 398 K (Figure 3C-b). A similar blue-shifted emission trend was also observed for **CuNC-11** (Figure 3C-d). The blue-shifting trend with increasing temperature hints at a TADF process for these two NCs.

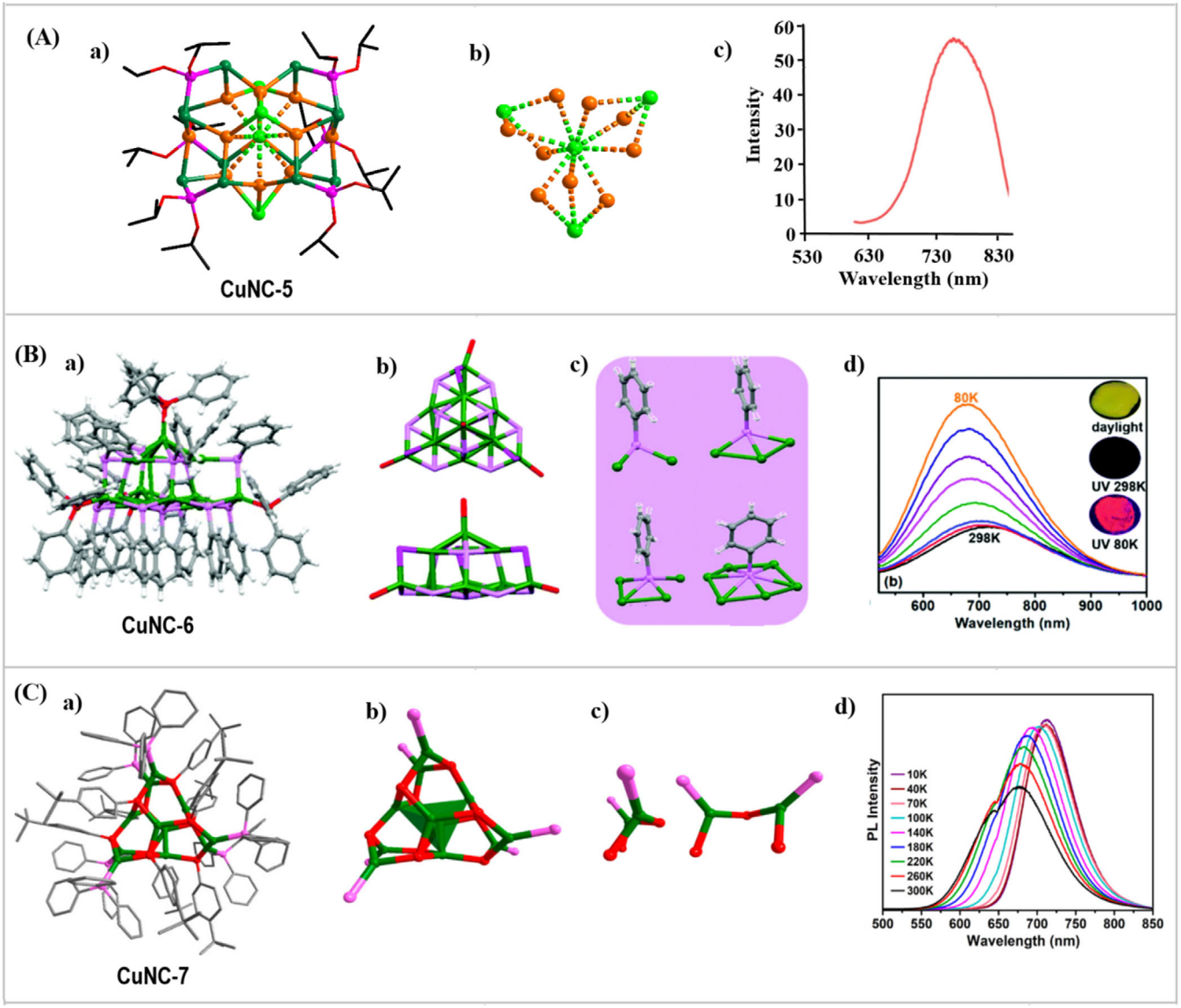

FIGURE 2 A: (a) Structure of **CuNC-5**. Color labels: green = I; cyan-blue = Se; orange = Cu; purple = P; black = C. (b) μ_9-I^- and μ_3-I^- ligands. (c) Emission spectrum in the solid state. Reproduced with permission.[21] Copyright 2017, American Chemical Society. B: (a) Structure of **CuNC-6**. Color labels: green = Cu; red = P; violet = Se; orange = S; gray = C; white = H. (b) Top and side view of the Cu_{13} skeleton. (c) Coordination modes of the $PhSe^-$ ligands. (d) Temperature-dependent emission in the solid state (inset: the pictures of the samples under different conditions, λ_{ex} = 365 nm). Reproduced with permission.[22] Copyright 2019, The Royal Society of Chemistry. C: (a) Structure of **CuNC-7**. Color labels: green = Cu; red = S; pink = P; gray = C. (b) $Cu_{11}S_9P_6$ framework. (c) Top and side view of the $Cu_2S_3P_2$ motif. (d) Temperature-dependent emission spectra. Reproduced with permission.[23] Copyright 2020, American Chemical Society

Considering that the singlet-triplet energy separation $\Delta E(S_1 - T_1)$ as a crucial parameter in TADF is generally required to be <3000 cm^{-1}/0.37 eV, the temperature-dependent lifetime decays were measured to calculate $\Delta E(S_1 - T_1)$. As a result, $\Delta E(S_1 - T_1)$ = 1200 cm^{-1}/0.15 eV, $\tau(T_1)$ = 25 μs and $\tau(S_1)$ = 14 ns were extracted for **CuNC-15**; for **CuNC-11**, $\Delta E(S_1 - T_1)$ = 380 cm^{-1}/0.047 eV, $\tau(T_1)$ = 33.5 μs and $\tau(S_1)$ = 115 ns were calculated. These values demonstrate that TADF took place with reverse intersystem crossing (RISC) from the triplet state T_1 to the singlet S_1. This is the first time that high-nuclearity CuNCs have been proven to exhibit TADF in the NIR region. These emissions were also assigned to originate from the ^{3}LMCT modified by cuprophilic interactions.

2.2 | AIE and/or CPL

AIE is an interesting photophysical phenomenon that was first observed in organic luminophores by Tang's group.[27] Fortunately, AIE is also a promising strategy to enhance the emission of metal NCs.[28] The AIE origin of CuNCs could be attributed to the restriction of the intramolecular vibration and rotation of the ligand shell of NCs after aggregation, which thereby facilitates the radiative energy transfer via restraining the non-radiative excited state relaxation. In practice, the common AIE approach for CuNCs is to use self-assembly to trigger the spatial arrangement of individual NCs into compact and highly ordered architectures.[28] For AIE-active CuNCs, this strategy involves the

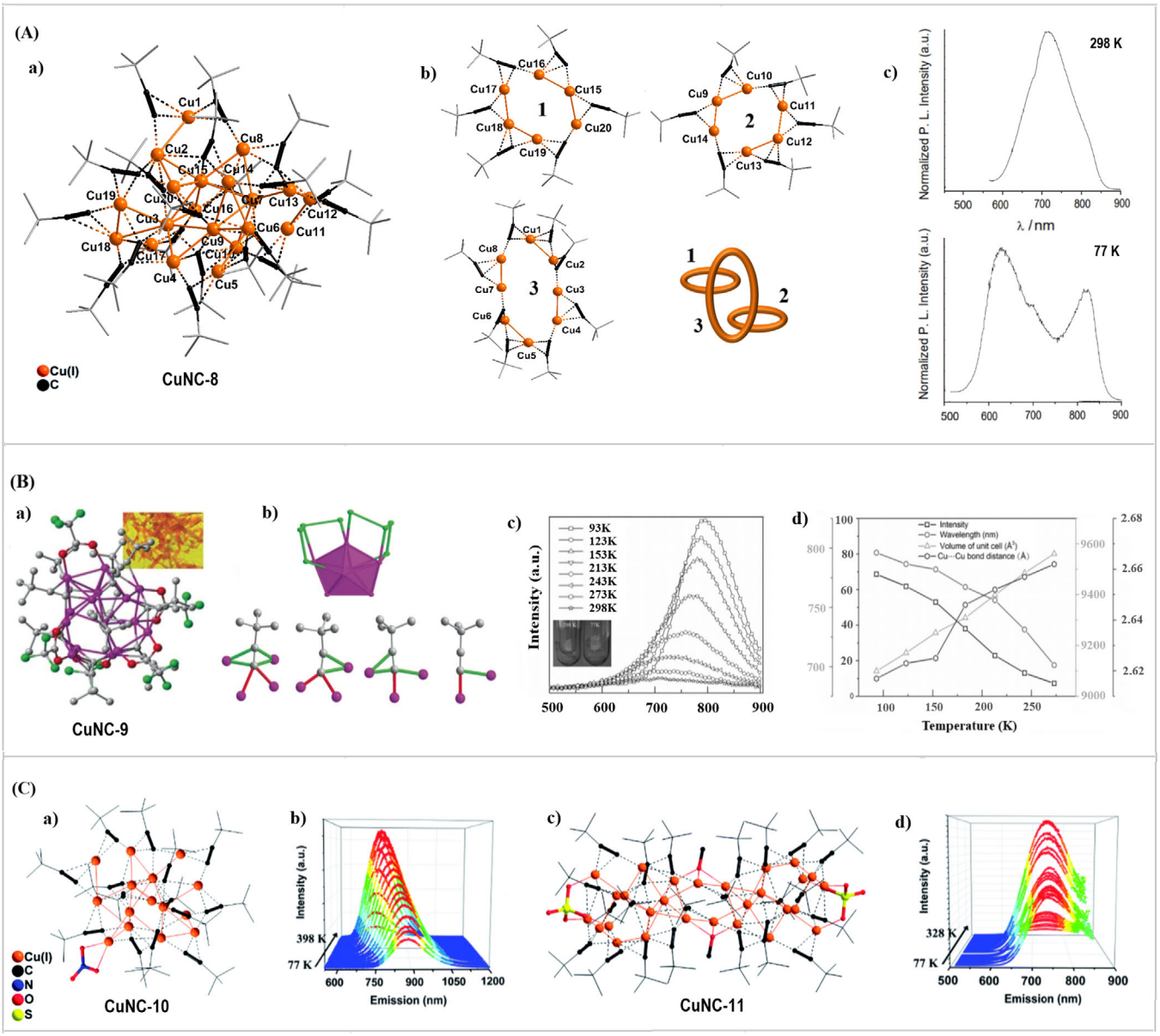

FIGURE 3 A: (a) Structure of **CuNC-8**. (b) Anatomy of the $Cu(I)_{20}$ cluster. (c) Emission spectrum. Reproduced with permission.[24] Copyright 2005, Wiley. B: (a) Structure of **CuNC-9**. Color code: purple, Cu; green, F; gray, C; red, O. (b) Cu_{15} core comprised of a pentagonal bipyramid rounded by two Cu_4 folding lines highlighted by green, and coordination modes of $^tBuC{\equiv}C^-$. (c) Temperature-dependent emission spectra. (d) The plots for variation trends of volume of unit cell, emission intensity, emission maximum, and mean Cu···Cu bond lengths as function of temperature. Reproduced with permission.[25] Copyright 2016, Wiley. C: (a) Structure and (b) temperature-dependent emission spectra of **CuNC-10**. (c) Structure and (d) temperature-dependent emission spectra of **CuNC-11**. Reproduced with permission.[26] Copyright 2019, The Royal Society of Chemistry

manipulation of the driving forces guiding the intercluster interactions, in which the attractive forces are usually the intermolecular interactions between surface ligands or motifs of different NCs and triggered by external stimuli such as solvents.

On the other hand, CPL constitutes an attractive luminescence phenomenon that provides the differential emission intensity of right and left circularly polarized light.[29] Briefly speaking, CPL originates from the chiral emissive excited states to offer information on the excited state properties of the chiral molecular systems. In the aggregate state or solid state, chiral couplings between the transition dipole moments operate, which could enhance the CPL property, as manifested in the increase of luminescence dissymmetry factor (g_{lum}).[30] In the field of CuNCs, introduction of CPL activity can be achieved by the extrinsic chirality of the peripheral chiral ligands, which is the most controllable and efficient approach. By this approach, the chirality of the deliberately chosen ligands is transferred to the resulting CuNC materials to generate CPL.

Zang et al. have utilized a pair of chiral alkynyl ligands, (R/S)-2-diphenyl-2-hydroxylmethylpyrrolidine-1-propyne (abbreviated as R/S DPM), to prepare an optically pure enantiomeric pair of $[Cu(I)_{14}(R/S\text{-}DPM)_8](PF_6)_6$ (**CuNC-12-R/S**).[31] **CuNC-12-R** is composed of a discrete distorted cubic $Cu(I)_{14}$ core and eight R-DPM ligands (Figure 4A-a). The $Cu(I)_{14}$ framework can be regarded as a distorted Cu_6^{6+} octahedron being encapsulated in the Cu_8^{8+} cube (Figure 4A-a). Seven alkynyl groups adopt a μ_3-η^1,η^1,η^2 ligation mode, and the remaining one takes a μ_2-η^1,η^2 mode, which relatively decreases the symmetry of the cluster, giving rise to a chiral metal core. **CuNC-12-R/S** are also CPL active,

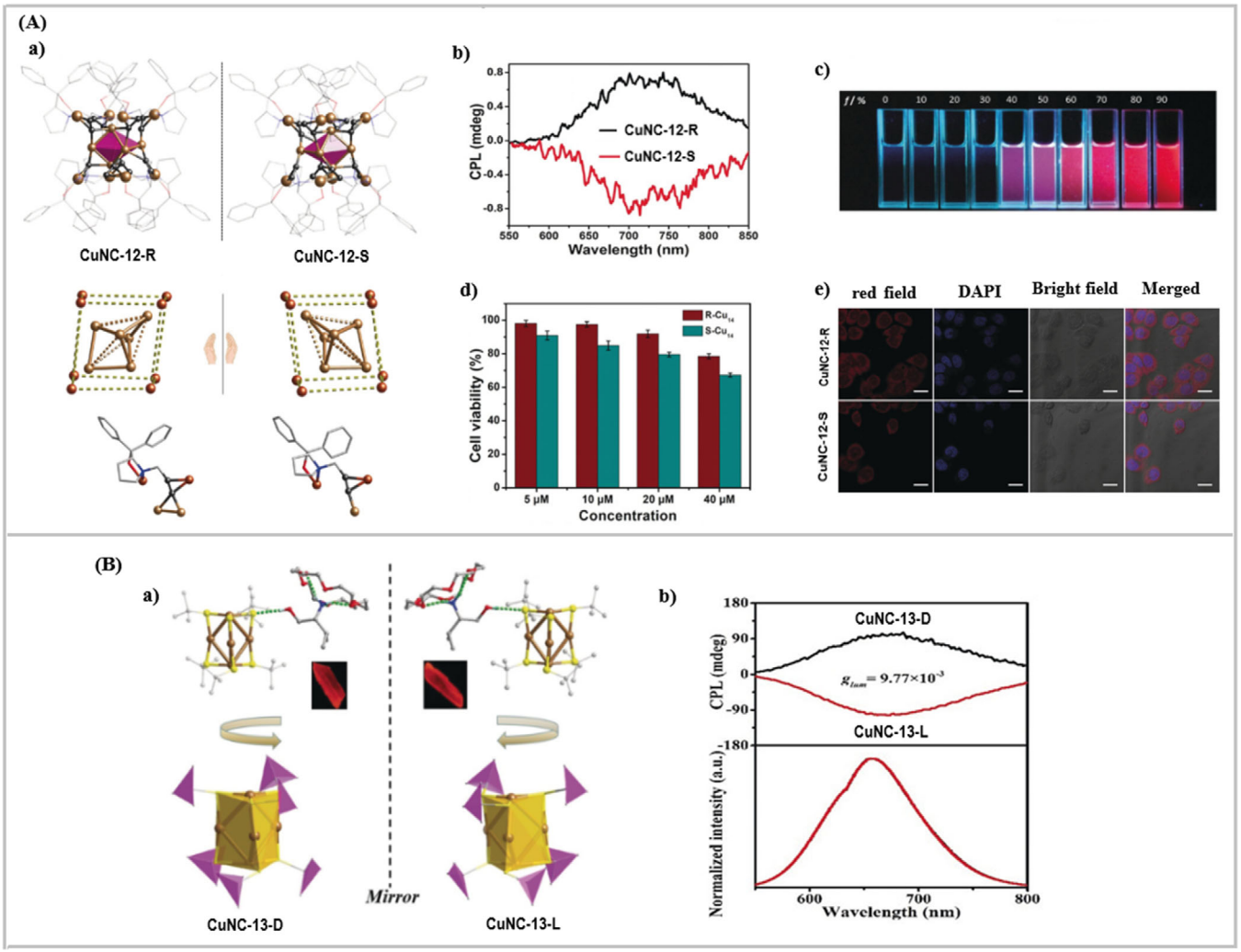

FIGURE 4 A: (a) Structures of **CuNC-12-R/S**, their $Cu(I)_{14}$ cores, and the coordination modes of alkynyl ligands. Cu brown/orange, O red, N blue, C gray; the carbon atoms of the ethynide group are represented as small black spheres. (b) CPL spectra of the enantiomers in the solid state. (c) Fluorescence photographs of **CuNC-12-R** in solutions with different fractions of *n*-hexane. (d) Viability of HeLa cells cultured with **CuNC-12-R/S** for 24 h. (e) Confocal images of HeLa cells incubated **CuNC-12-R/S** for 24 h. Red **CuNC-12-R/S**; blue nucleus. Scale bars: 25 μm. Reproduced with permission.[31] Copyright 2020, Wiley. B: (a) Structures of **CuNC-13-D/L**, and (b) their emission and CPL spectra. Color code: brown, Cu; yellow, S; green, H; gray, C; red, O; blue, N. Reproduced with permission.[32] Copyright 2019, Wiley

in which the CPL in the solid state responded at 726 nm with a g_{lum} of approximately 3.0×10^{-3} (Figure 4A-b). Furthermore, the AIE activities of these NCs were explored by analysis of the emission of **CuNC-12-R** in a DCM/*n*-hexane solvent system (Figure 4A-c). As observed, the dilute solution of **CuNC-12-R** in DCM was completely non-emissive; a very weak red emission appeared when the volume fraction of *n*-hexane $f = \text{vol}_{n\text{-hexane}}/\text{vol}_{n\text{-hexane+DCM}}$ increased to 40% and the emission exhibited a further enhancement upon further increasing the *n*-hexane fraction. When *f* increased to 90%, the solution showed a strong red emission with a quantum yield of 1.6%, suggesting the presence of well-dispersed colloids of denser aggregates. Crystallization- and aggregation-induced emission (CIE and AIE respectively) contribute to the occurrence of the CPL of **CuNC-12-R/S** in the crystalline and aggregated states, respectively. Based on the red emission and AIE characteristics, **CuNC-12-R/S** has also been tested for bioimaging. As shown in Figure 4A-d, the cytotoxicity of **CuNC-12-R/S** was examined with a standard CCK-8 assay in vitro. **CuNC-12-R** was more cytotoxic than **CuNC-12-S**, which could be ascribed to a stereospecific interaction between the chiral nanoparticles and cells. When HeLa cells and NG108-15 cells were treated with 5 μm **CuNC-12-R/S** in cell medium for 24 h, the confocal microscopy images suggest that the NCs with red luminescence were found to be distributed throughout the cytoplasm of both cell types (Figure 4A-e). These results demonstrate that **CuNC-12-R/S** can be a potential agent for biolabeling.

Zang et al. also prepared a pair of enantiomers, namely, $[\text{D/L-valinol(18-crown-6)}]^+[Cu_5(S^tBu)_6]^-$ (**CuNC-13-D/L**). **CuNC-13-D/L** crystallized in the chiral orthorhombic $P2_12_12_1$ space group, in which **CuNC-13-D/L** consists of the anionic $[Cu_5(S^tBu)_6]^-$ unit and counter ion of $[\text{D/L-valinol(18-crown-6)}]^+$ (Figure 4B-a).[32] The cationic amino alcohols are fixed by H-bonds (N—H···O) between the $-NH_3^+$ group and oxygen atoms of 18-crown-6 moieties and connected with anionic $[Cu_5(S^tBu)_6]^-$ clusters by O—H···S hydrogen bonds, which induces the orthorhombic chiral $P2_12_12_1$ space group. Once again, the emission and CPL spectra were recorded for this pair of enantiomers (Figure 4B-b). This work provides an avenue to understand how the self-assembly process induces chiral metal NCs and impact their emission property.

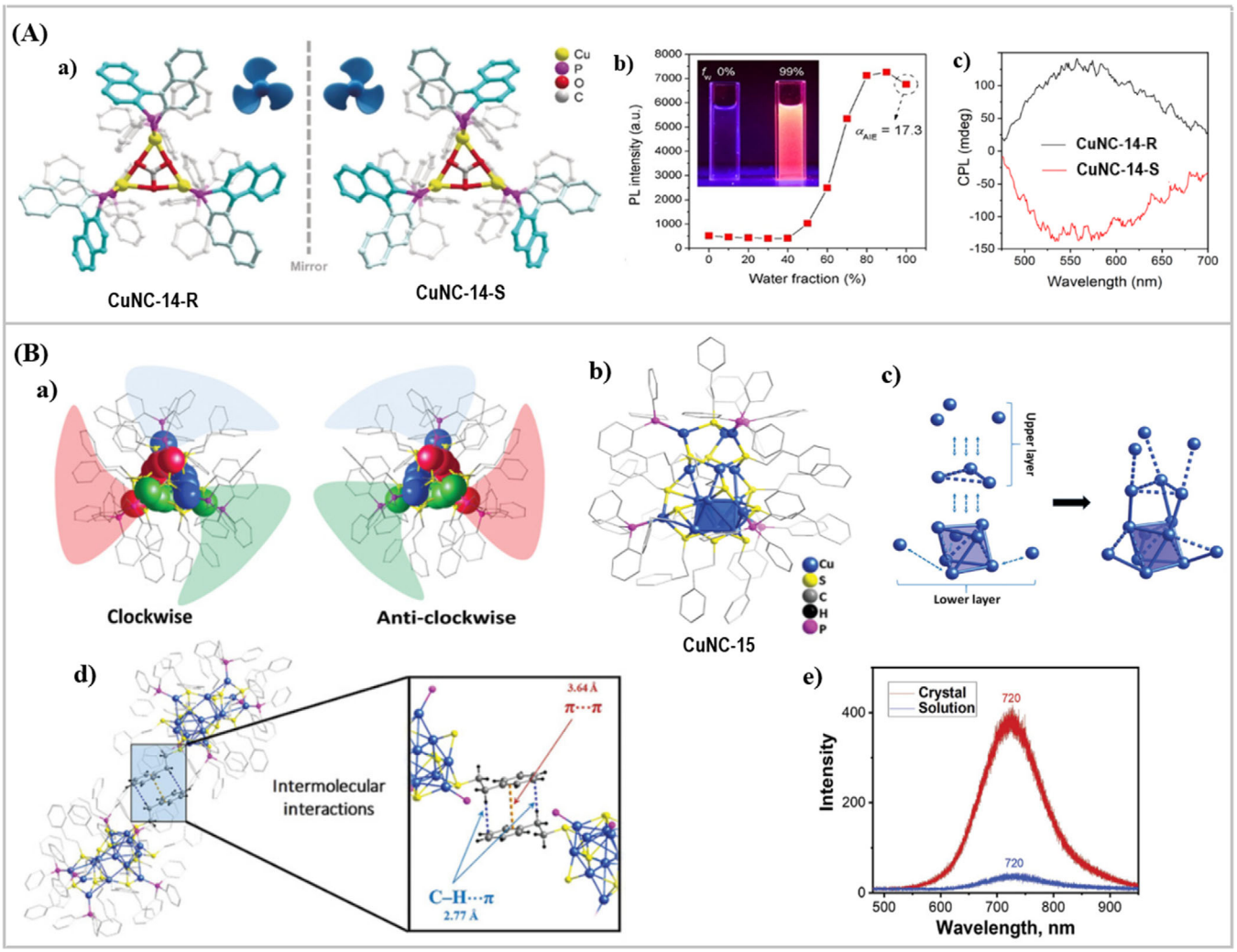

FIGURE 5 A: (a) Structures of **CuNC-14-R/S**. (b) Luminescence intensity at 605 nm as a function of f_w. (c) CPL spectra of the enantiomers. Reproduced with permission.[33] Copyright 2020, Wiley. B: (a) Top view of one pair of enantiomers of **CuNC-15**. (b) Structure of **CuNC-15**. (c) Anatomy of the Cu_{15} skeleton. (d) Intermolecular interactions between **CuNC-15** molecules. (e) Emission spectra of **CuNC-15** in crystalline and solution forms. Reproduced with permission.[34] Copyright 2021, Wiley

In another study, Zang group has prepared a pair of chiral trinuclear NCs of $[Cu(I)_3(R/S\text{-}BINAP)_3CO_3]({}^tBuSO_3)$ (**CuNC-14-R/S**), where BINAP = 2,2-*bis*(diphenylphosphino)-1,1-binaphthyl.[33] The central carbonate unit ligates with three Cu(I) atoms, each in the bidentate mode, to form a $Cu(I)_3$ triangle (Figure 5A-a). Each Cu(I) is also coordinated by a bidentate R/S-BINAP ligand. The arrangement of R/S-BINAP ligand around the $[Cu_3CO_3]^-$ core forms an intriguing three-bladed propeller-like structure (Figure 5A-a). Employment of BINAP ligands has conferred **CuNC-14-R/S** with intriguing properties. First, the phenyl groups of BINAP ligands underwent intramolecular rotation in the solution to quench the luminescence of the NCs. Nevertheless, such rotational motion was restricted in the solid state to produce strong CC and MLCT emissions (Figure 5A-b), which make **CuNC-14-R/S** AIE luminogens. This is the so-called restriction of intramolecular motion mechanism. Second, the chiral structure and intense luminescence of BINAP endow **CuNC-14-R/S** with CPL property, where a remarkable g_{lum} of 2×10^{-2} was obtained (Figure 5A-c).

Bakr et al. have reported $[Cu(I)_{15}(PPh_3)_6(PET)_{13}](BF_4)_2$ (**CuNC-15**, PET = 2-phenylethanthiol), as shown in Figure 5B-b.[34] The $Cu(I)_{15}$ skeleton can be divided into two parts: a lower layer of a distorted trigonal antiprismatic Cu_6 core extended by three symmetrically located Cu atoms at the bottom trigonal face; and an upper layer of two Cu_3 triangles (Figure 5B-c). This kind of Cu(I) skeleton has not been observed in the previous reports of coinage metal NCs. As shown in Figure 5B-b, the thiolate ligands bind to the Cu(I) skeleton by adopting two ligation modes of μ_3-η^1, η^1, η^1 and μ_2-η^1, η^1. In addition, phosphine ligands are associated with the skeleton. The entire structure adopts a C_3 symmetry and constitutes a "tri-blade fan" configuration, where the enantiomers are classified into clockwise and anticlockwise structures (Figure 5B-a). Weak intermolecular ligand interactions including C–H···π and π-π stacking play a crucial role in controlling and stabilizing the surface structure. As shown in Figure 5B-d, C–H···π interactions and π-π stacking interactions are responsible for the centrosymmetric supramolecular dimer formation (Figure 5B-d) adopted by the two opposite enantiomers. Based on the weak intermolecular interactions to limit the vibrational and rotational movement of ligands, **CuNC-15** demonstrates a CIE enhancement (CIEE) behavior. As a result, this allows observation of the CIEE phenomenon (Figure 5B-e), where the NC

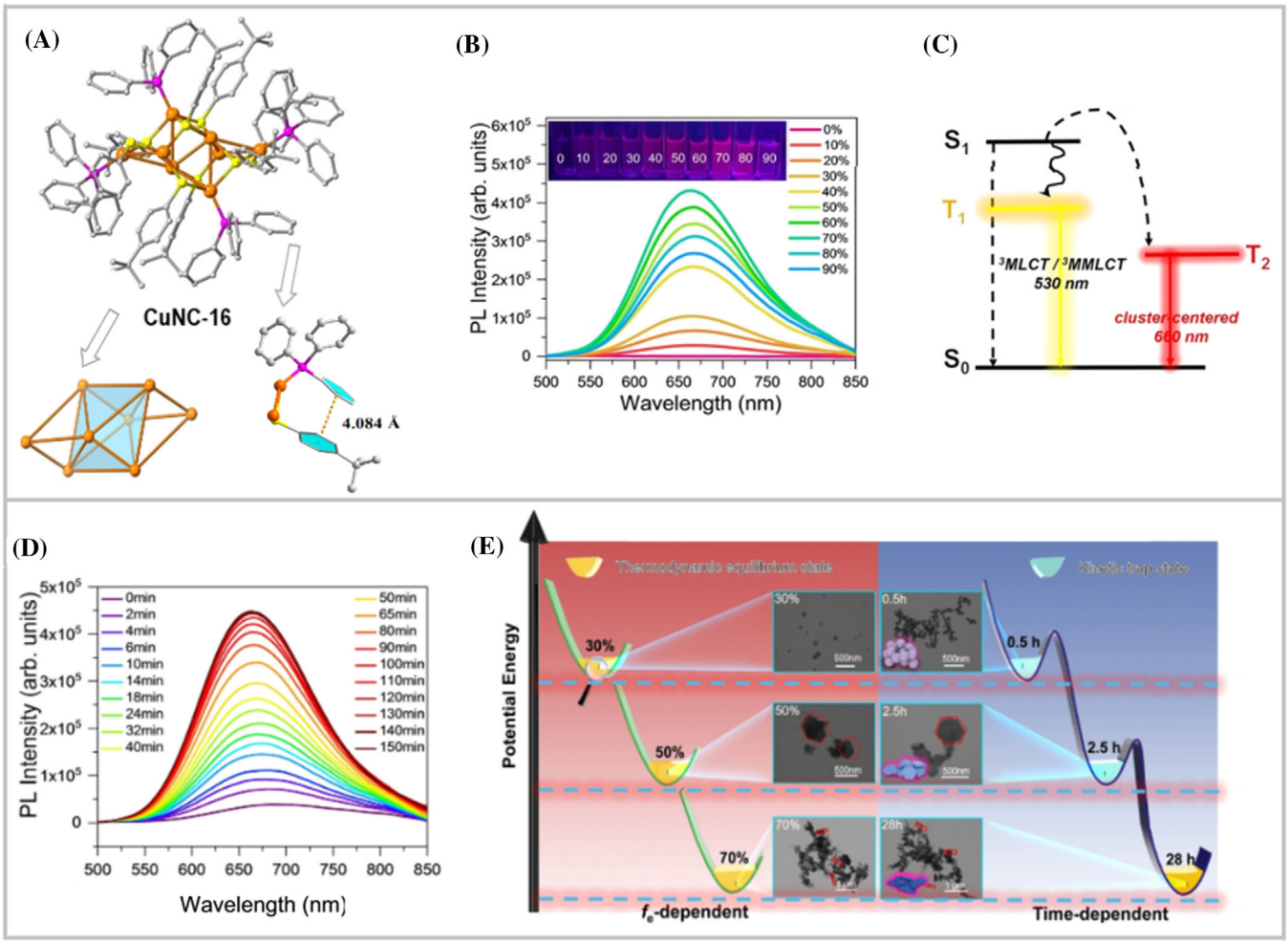

FIGURE 6 (A) Structure of **CuNC-16** with its $Cu(I)_8$ skeleton and the $\pi\cdots\pi$ interactions between PPh_3 and $^tBuC_6H_4S^-$ shown. Color labels: orange, Cu; pink, P; gray, C; yellow, S. (B) Emission spectra and photographs of **CuNC-16** in EtOH/DCM with different f_e. (C) Schematic diagram of the excited state relaxation dynamics. (D) Time-dependent fluorescence spectra of **CuNC-16** in EtOH/DCM with f_e = 70%. (E) Energy landscape of kinetic traps versus thermodynamic equilibrium states. The black line represents the kinetic traps process of f_e = 70%. The green line represents the thermodynamic equilibrium state under different f_e systems. Inset: the morphological features. Reproduced with permission.[35] Copyright 2022, Wiley

in the crystalline state exhibits a bright emission in the NIR region at 720 nm, and the emission intensity (PLQY = 3.2%) is 30 times higher than that in solution (PLQY = 0.1%).

Very recently, Sun et al. reported $[Cu(I)_8(^tBuC_6H_4S)_8(PPh_3)_4]$ (**CuNC-16**).[35] The $Cu(I)_8$ skeleton features a twisted $Cu(I)_6$ octahedron with two additional Cu(I) atoms capped on two opposite triangles (Figure 6A). There are weak cuprophilic interactions within the $Cu(I)_8$ structure, which contribute to the metal cluster-centered (CC) transition state. Two different coordination modes of μ_2 and μ_3 were found for the eight $^tBuC_6H_4S^-$. In addition, there is a $\pi\cdots\pi$ contact of 4.084 Å between the PPh_3 and $^tBuC_6H_4S^-$ ligand within **CuNC-16**, which provides a good driving force for supramolecular assembly to dictate AIE. The degree of aggregation of **CuNC-16** depends on the volume fraction of ethanol in the mixture of DCM and EtOH, $f_e = vol_{EtOH}/vol_{EtOH+DCM}$. The kinetically controlled assembly process of **CuNC-16** yields a thermodynamically stable aggregate (TSCA). In exploration of the AIE property, the emission intensity of TSCA first increases and then decreases with the increase of f_e from 40% to 90% (Figure 6B). The diverse f_e systems present lifetimes in microsecond scale, which hints at the CC and CT emission mechanisms (Figure 6C). The diverse degree of aggregation of TSCA leads to different packing compactness of **CuNC-16** to give distinct nanoscale assemblies. When f_e is lower than 30%, flexible nanoparticles are obtained, and transformed into "quasi-hexagon" (f_e∈[30%, 50%]), and then to nanosheets (f_e∈[50%, 70%]). The nanosheets are again transformed into "thorny" nanoparticles that adhere to each other (f_e∈[70%, 90%]). To further investigate the kinetically controlled **CuNC-16** assembly (KCCA), time-dependent emission spectroscopy was used to monitor the f_e = 70 % system (KCCA-1). As seen in Figure 6D, the emission intensity of KCCA-1 located at 660 nm gradually increased with time, accompanied by a 10 nm blue shift. Furthermore, KCCA-1 experienced the concerted "nucleation" (t = 0–60 min) and "assembly" (t = 60–150 min) processes, as testified by TEM (Figure 6E). KCCA-1 aggregated to minimize the surface energy and formed flexible nanoparticles (t = 0–30 min), which is analogous to the structure of TSCA with f_e lower than 30%. In the range of 60–150 min, KCCA-1 gradually evolved into a "quasi-hexagon" accompanied by the degradation of nanoparticles, which resembles the result of TSCA at f_e = 50 %. The "quasi-hexagon" evolves into nanosheets (t = 28 h) as the thermodynamically stable state.

Zhang et al. have revealed the significant enhancement of luminescence intensity for $[Cu(0)_4Cu(I)_{10}DT_{10}]$ (**CuNC-17**)

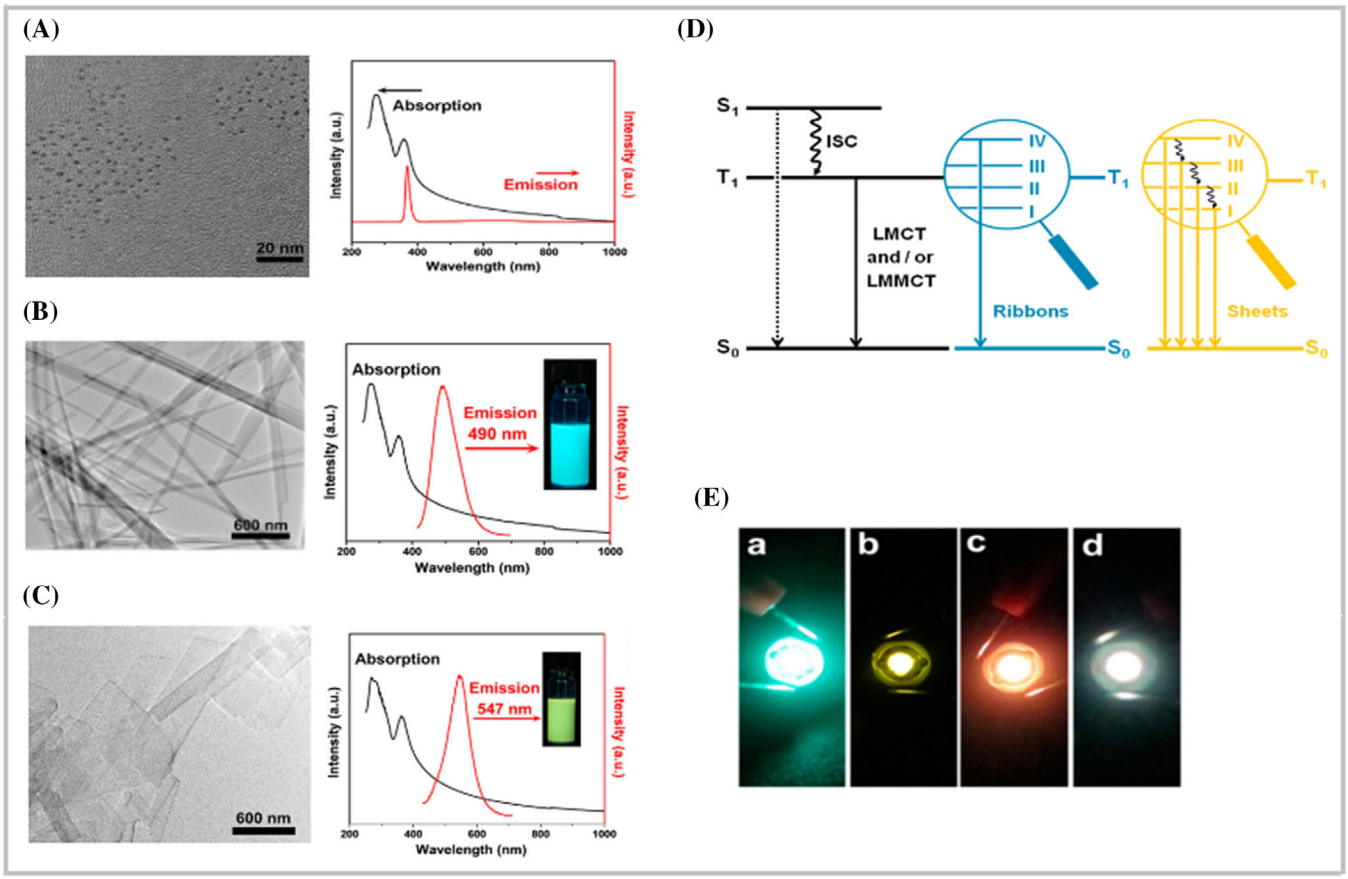

FIGURE 7 TEM image of (A) individual NCs of **CuNC-17**, (B) ribbons, and (C) sheets. Their steady-state absorption and emission spectra in chloroform are shown. Inset: the fluorescent image under excitation at 365 nm. (D) Energy level of ribbons and sheets. (E) Fluorescent images of the LEDs from CuNC self-assembled (a) ribbons, (b) sheets, and (c) AuNC sheets; (d) fluorescent image of the WLED from ribbons, sheets, and AuNC sheets. Reproduced with permission.[36] Copyright 2015, American Chemical Society

by using self-assembly to enhance its aggregation degree.[36] As shown in Figure 7A, the individual NCs of **CuNC-17** with an average diameter of 1.9 ± 0.2 nm were initially prepared, which is non-emissive under excitation at 365 nm. Subsequently, self-assembly strategy was applied to direct the NCs into one-dimensional ribbons featuring an average width of about 50–200 nm (Figure 7B). The ribbons display a strong blue-green emission centered at 490 nm with a full width at half-maximum (FWHM) of around 86 nm. Furthermore, the as-synthesized two-dimensional sheet assembles show an average width of about 200–800 nm (Figure 7C). In contrast, the sheet assembles show a yellow emission peaking at 547 nm with a FWHM of around 84 nm, and decreased emission intensity. To briefly interpret the self-assembly induced AIE, the original non-luminescent **CuNC-17** exhibits a strong emission after forming compact and ordered assemblies. The improved compactness of **CuNC-17** from individual NCs to ribbons reduces the non-radiative relaxation of excited states to display enhanced emission intensity (Figure 7D). Meanwhile, self-assembly induces inter-NC cuprophilic interactions to increase the average Cu(I)···Cu(I) distance, generating a blue-green emission. As the sheets show loose NCs arrangement, the inter-NC cuprophilic interactions are weaker than that of ribbons to decrease the average Cu(I)···Cu(I) distance, thus decreasing the emission energy to give a red-shifted emission. More surprisingly, these NCs assemblies have been used as the phosphors in the color conversion layer for fabricating LEDs because of their strong emissions. As seen in Figure 7E, mixing CuNC ribbons or sheets with the polydimethylsiloxane precursors, and depositing on commercially available GaN LED chip, gives LED devices with blue-green and yellow emissions, respectively. Very impressively, CuNC ribbons with blue-green emission, CuNC sheets with yellow emission, and AuNC sheets with red emission are mixed in a ratio of 1.2/1/1.5 to produce a WLED (white light emitting diode). This represents an unprecedented example to employ metal NCs to fabricate WLED.

Zhang et al. have also provided a new perspective to investigate the AIE origin, wherein they used a liquid–liquid phase reaction system to initiate the self-assembly of **CuNC-17** into ultrathin nanosheets, which feature significant metal defects-rich surface.[37] It was observed that the emission of the ultrathin nanosheets (Figure 8A) blue-shifts from 550 to 517 nm from 298 to 77 K, (Figure 8B), along with the increase of emission intensity. Meanwhile, a new emission peak upon cooling appears at 490 nm and shifts to 517 nm at 77 K. This indicates the coexistence of two emission states for the nanosheets. In stark contrast, the block assemblies with minimized metal defects exhibit only one band at 490 nm in the temperature-dependent emission measurement. It is thus postulated that the T_1 state at 490 nm is the real LMMCT-determined triplet state, while the metal defects of nanosheets provide a lower metal energy level leading to the red-shifted emission at 550 nm from the T_2 state (Figure 8C). First, the metal defects-rich nanosheets possess increased

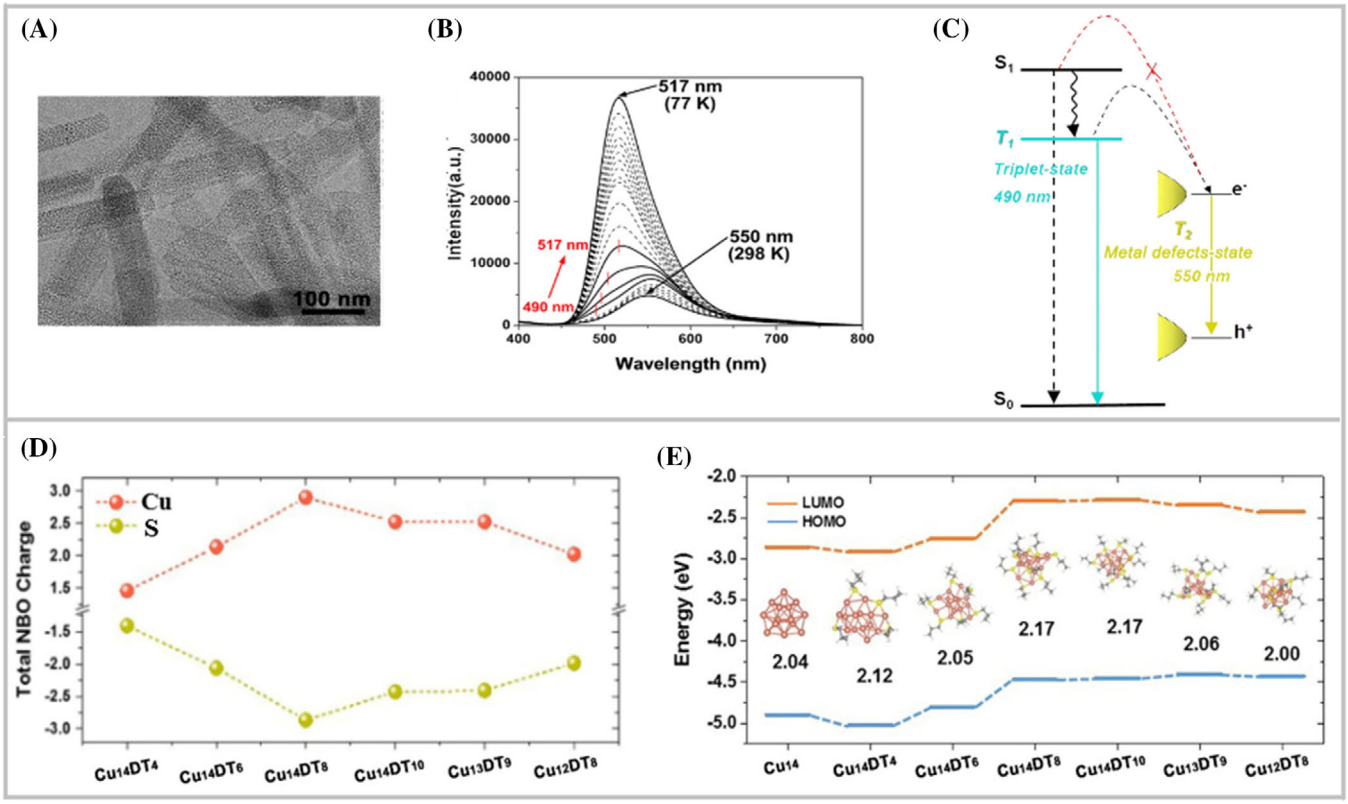

FIGURE 8 (A) TEM images of self-assembled nanosheets from NCs of **CuNC-17**. (B) Temperature-dependent emission of the nanosheets from 77 to 298 K. (C) Schematic diagram of the excited state relaxation dynamics of the nanosheets. (D) Total charge populations of Cu and S atoms in Cu_x-DT_y clusters obtained by NBO analysis, where *x* and *y* represent the number of Cu and DT, respectively. (E) Optimized structures and frontier orbital energies of the Cu_x-DT_y clusters. Reproduced with permission.[37] Copyright 2017, American Chemical Society

Cu(I)-to-Cu(0) ratio to facilitate the radiative relaxation of excitons to yield emission enhancement. Second, as suggested by charge distribution by natural bond orbital (NBO), the larger NBO charge of Cu and S atoms is observed for the Cu_{14}-DT_8 and Cu_{13}-DT_9 with less coverage, which promotes charge separation to enhance the emissions (Figure 8D). Furthermore, DFT calculation indicates that once one or two Cu atoms and/or DT ligands are missing in the $Cu_{14}DT_{10}$ clusters which generate Cu_{13}-DT_9 and/or Cu_{12}-DT_8, the bandgap is slightly narrowed and more close to the Cu_{14}-DT_6 with less coverage (Figure 8E).

3 | APPLICATIONS OF CuNCs

The understanding of the atomically precise structures of CuNCs not only provides an impactful insight into the properties of these metal NCs but also lays a basis to explore their functional applications. In line with this, efforts have been devoted to exploring their potential applications in CO_2 ERR, chemical sensing, catalysis in organic synthesis, and electronic devices.

3.1 | CO_2 ERR

CO_2 ERR refers to the catalyst-promoted conversion of CO_2 to new carbon molecules such as CO, HCOOH, CH_4, and other hydrocarbons.[38] From both environmental and economic viewpoints, CO_2 ERR is highly desirable not only to alleviate the global warming effect, but also to convert the excessive CO_2 into value-added chemicals. While CO_2 itself is stable and relatively inert, efforts have been devoted themselves to develop catalysts for facile conversion of CO_2 to the desired products.[39] In this respect, exploration of Cu(I) hydride NCs as catalysts for CO_2 ERR has several advantages: 1) Cu(I) hydride NCs have capping and interstitial hydrides that are favorable for binding CO_2. Such favorable binding interaction is attributed to the attraction between the negatively charged hydride and the positively charged carbon of CO_2, which can easily initiate the CO_2 reduction reaction. 2) The negatively charged hydride facilitates the formation of the HCOO* intermediate, thus releasing HCOOH instead of CO as the product, which offers a new pathway to study the product selectivity. 3) In contrast with the bulk metal surfaces and nanoparticles, Cu(I) hydride NCs exhibit atomically precise structures, which can provide an opportunity to explore the catalytic process and mechanism.[40]

Practically, hydrides are located at the capping surface and the interstitial positions of the metal core to stabilize Cu(I) NCs. Unambiguous characterization of hydrides has been a tricky task, where neutron diffraction, ^{1}H NMR, high-resolution electrospray-ionization mass spectrometry (HR-ESI-MS), and DFT calculations have been employed to testify the presence of hydrides.[41] It is impressive that in 2021, a deep-learning approach developed by computational intelligence has been reported to pinpoint the location of hydrides.[42] As shown in Figure 9A, Jiang et al. have created a three-dimensional convolutional neutral network (3D-CNN) based on 23 reported crystal structures, the

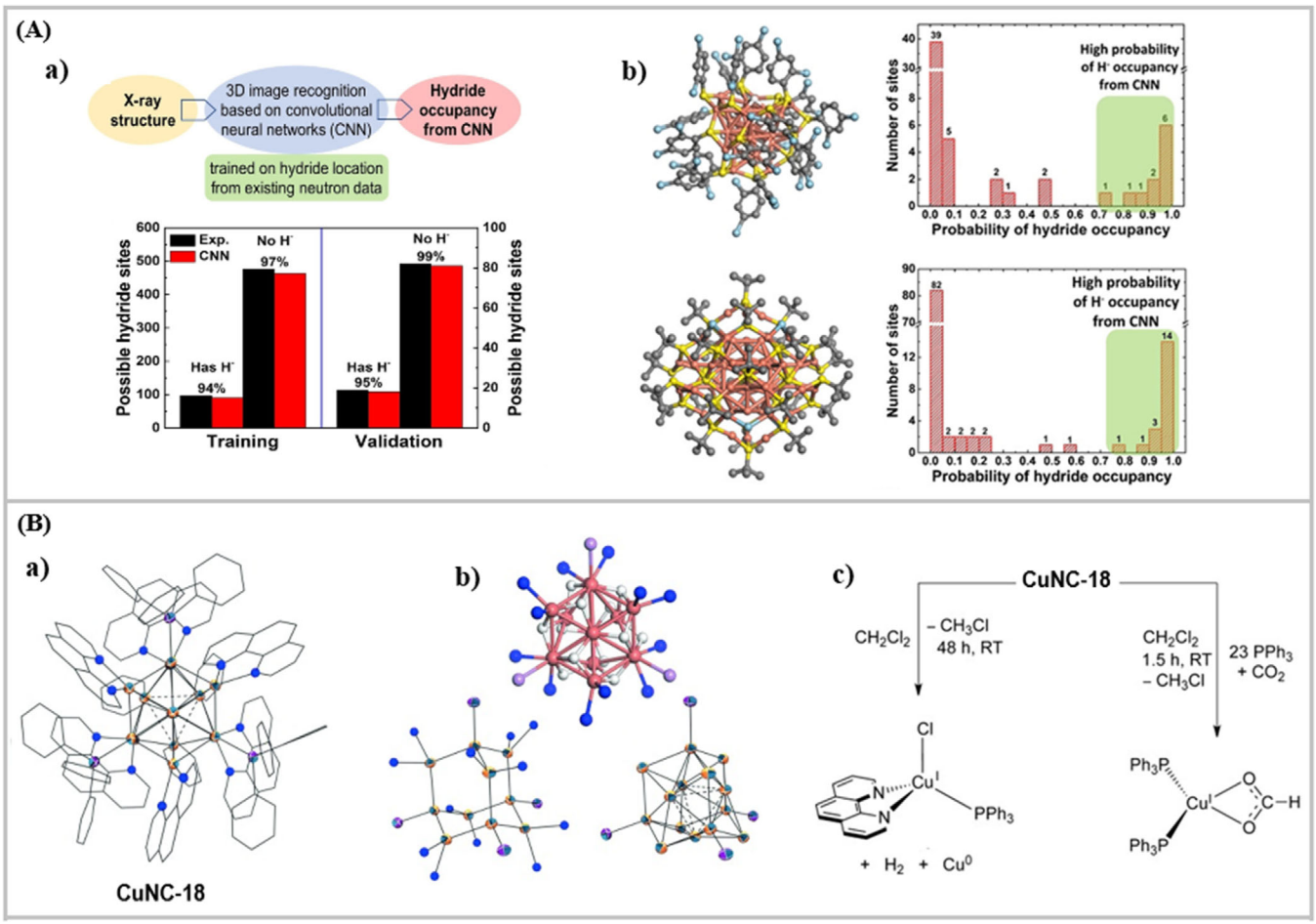

FIGURE 9 A: (a) Workflow of using CNN to predict hydride location. (b) Application of CNN to predict hydride locations in NCs of $[Cu_{25}H_{10}(SPhCl_2)_{18}]^{3-}$ (upper) and $[Cu_{61}(S^tBu)_{26}S_6Cl_6H_{14}]^+$(lower). Reproduced with permission.[42] Copyright 2021, Wiley. B: (a) Structure of **CuNC-18**. Color legend: copper = yellow-orange; hydrogen = white; phosphorus = fuchsia; nitrogen = blue. (b) Optimized structure determined by the PW91 functional to show the μ_3-H environments (upper). Diamondoid arrangement of the outer Cu shell and ORTEP diagram of **CuNC-18** with carbon, nitrogen, chloride, and hydrogen atoms removed (lower). (c) Reactivity of **CuNC-18** with CO_2 and CH_2Cl_2, the former of which gives a formate-containing species. Reproduced with permission.[43] Copyright 2015, Wiley

hydride positions of which have been confirmed by neutral diffraction. Capitalized on this CNN method, the possibility of hydride location in a CuNC can be thoroughly calculated. Next, by applying the symmetry of the Cu kernel to the possible hydride frameworks, those with the same symmetry can be picked out. Then, by taking the NC stability into consideration using DFT calculations, the most plausible hydride framework will stand out. It is expected that this computational methodology can accurately predict the hydride positions, which is highly important for a better understanding of both the structures and properties of Cu hydride NCs.

In fact, Cu(I) hydride NCs were initially found to react with CO_2 to give formate-containing complexes, as exemplified by $[Cu(I)_{14}H_{12}(phen)_6(PPh_3)_4][Cl]_2$ (**CuNC-18**, phen = 1,10-phenanthroline) reported by Hayton.[43] As shown in Figure 9B-a, **CuNC-18** features a tetrahedral $[Cu_4]^{4+}$ core, which is connected through Cu(I)···Cu(I) bonds to a diamondoid arrangement of ten Cu(I) atoms (Figure 9B-b). These ten Cu(I) atoms are coordinated by four PPh_3 ligands arranged at the corners of a tetrahedron, and six phen ligands arranged at the corners of an octahedron. As a result of such arrangement, **CuNC-18** features four hexagonal faces, wherein each face is situated opposite to a Ph_3P ligand. PW91 functionals illustrate that the twelve hydride ligands coordinate to the hexagonal copper faces, where each hydride ligand features a μ_3 coordination mode (Figure 9B-b). As seen in Figure 9B-c, **CuNC-18** shows reactivity with CO_2 to yield $[Cu(I)(Ph_3P)_2(k^2\text{-}OOCH)]$, which has laid a foundation for their catalytic applications in CO_2 ERR.

Liu, Lee, and Jiang et al. reported the first example of CO_2 ERR by a Cu(I) hydride nanocatalyst in 2017.[44a] As shown in Figure 10A-a, $[Cu(I)_{32}H_{20}\{S_2P(O^iPr)_2\}_{12}]$ (**CuNC-19**) consists of thirty-two Cu atoms, twelve $\{S_2P(O^iPr)_2\}^-$ ligands, and twenty hydrides. Figure 10A-b shows the anatomy of the $Cu(I)_{32}$ skeleton as a distorted hexacapped rhombohedral core of fourteen Cu atoms sandwiched between two triangular cupola fragments of (2 × 9) Cu atoms.[44b] Connecting the hexagonal bases of the two nestlike triangular cupola fragments generates an elongated triangular gyrobicupola. As seen in Figure 10A-a, the neutron diffraction study of **CuNC-19** clearly defines the position of twenty hydrides: μ_3-H (6 + 6 = 12), μ_4-H (2 + 4 = 6), and μ_5-H (2). Six μ_3-H ligands cap six of the eight Cu_3 triangles of both cupolae. The other six μ_3-H ligands bridge Cu_3 triangles of the hexacapped rhombohedron. Two μ_4-H ligands, each located at the center of one cupola, lie in a tetrahedral cavity formed by one interior capping Cu atom of the hexacapped rhombohedron and an apical Cu_3 triangle. The remaining four μ_4-H ligands and two μ_5-H ligands are located at the two

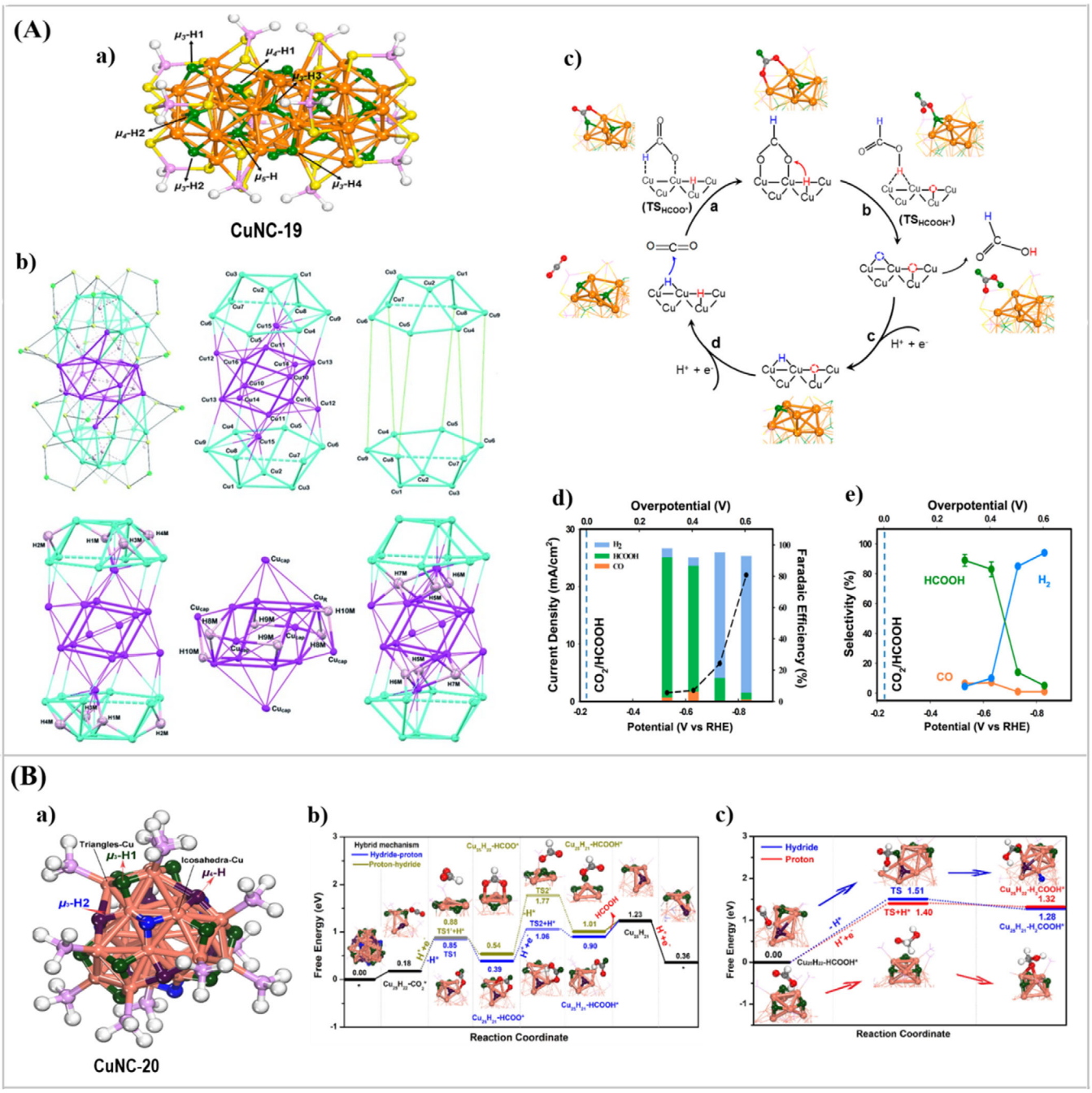

FIGURE 10 A: (a) Structure of **CuNC-19**. Color code: orange, Cu; green, hydride; yellow, S; purple, P; white, H. (b) Structure anatomy of **CuNC-19** without hydrides (upper) and with hydrides (lower). Color code: Cu cyan and magenta, S yellow, P green, H pink. (c) Proposed mechanism of **CuNC-19** as catalyst in CO_2 ERR to generate HCOOH. (d) Current densities and cumulative Faradaic efficiencies to produce H_2, HCOOH, and CO. (e) Product selectivity at different overpotentials. Reproduced with permission.[44a] Copyright 2017, American Chemical Society. Reproduced with permission.[44b] Copyright 2015, Wiley. B: (a) Structure of **CuNC-20**. Color modes: orange for Cu, lavender for P, white for H at the phosphine ligands, and green, dark purple, blue for the hydrides, highlighted in arrows. (b) Reaction scheme of **CuNC-20** via hybrid mechanism in CO_2 ERR to produce HCOOH. (c) Hydride/proton mechanism of HCOOH reduction to give H_2COOH. Reproduced with permission.[48] Copyright 2020, Elsevier

interfaces between the hexacapped rhombohedron and the cupolae. **CuNC-19** is the first example exhibiting tri-, tetra-, and pentacoordinated hydrides in capping and interstitial modes.

Figure 10A-d,e shows the experimental results of CO_2 ERR based on **CuNC-19**. As can be seen from Figure 10A-d, the average current density during 90 min of controlled potential electrolysis (CPE) becomes significant at the overpotential of 0.3 V and increases with overpotential. Figure 10A-d also shows the cumulative Faradaic efficiency of the product formation after 90 min of CPE at different overpotentials: H_2, HCOOH, and CO were detected as the main products accounting for the cumulative Faradaic efficiency of >90%. The selectivity of these three products is compared as a function of overpotential in Figure 10A-e. **CuNC-19** predominantly produces HCOOH at low overpotentials (89% at 0.3 V and 83% at 0.4 V). By contrast, the product selectivity dramatically changes when the overpotential is higher than 0.5 V where H_2 is predominantly produced (85% at 0.5 V and 94% at 0.6 V). These experimental results are in excellent agreement with our DFT prediction that HCOOH formation is favored at low overpotential, while

HER dominates at a higher overpotential. We further analyzed the turnover number of the **CuNC-19** for HCOOH production and found it to be 1740 mol of HCOOH per mole of **CuNC-19** after 90 min of CPE, supporting the replenishment of the lattice hydrides during the CO_2 reduction. For comparison, Cu(0) nanoparticles produced mainly CO at low overpotentials,[45] while Cu foil produced mainly H_2 at low overpotentials.[46]

The mechanism for HCOOH production was proposed in Figure 10A-c. DFT calculations show that among the twenty hydrides, the exposed capping μ_3-H1 hydride has the most favorable binding for the CO_2 molecule, with a binding strength of −0.24 eV. Initially, the μ_3-H1 hydride is first added to C to form $Cu_{32}H_{19}L_{12}$-HCOO. Notably, the two O atoms of the HCOO* intermediate are strongly bonded to the surface Cu, forming a five-membered ring. HCOO* subsequently reacts with μ_4-H1 to release the HCOOH product. The resulting $Cu_{32}H_{18}L_{12}$ cluster with two hydride vacancies then proceeds through the proton-reduction processes to refill the two lattice-hydride sites. Impressively, during HCOOH formation, the local structure of the Cu atoms around the two reacting hydrides does not change much, even after the loss of the interstitial μ_4-H1. This indicates that the structural stability of the Cu cluster framework can accommodate the loss of the interstitial hydrides, thereby facilitating the lattice-hydride mechanism to produce HCOOH. This report has provided a fundamental basis to exploit the activity, selectivity, and mechanism of Cu(I) hydride NCs for CO_2 ERR.

In 2015, Hayton et al. reported $[Cu(I)_{25}H_{22}(PPh_3)_{12}]Cl$ that is constructed from a Cu_{13} centered-icosahedron and formally features partial Cu(0) character.[47] Tang et al. have recently simulated its CO_2 ERR mechanism by using the simplified formula $[Cu(I)_{25}H_{22}(PH_3)_{12}]Cl$ (**CuNC-20**) for computational feasibility study (Figure 10B-a).[48] According to the DFT calculations, the hydrides and the $Cu(I)_{25}$ core play a synergistic role to dictate the selective reduction of CO_2 to HCOOH. As shown in Figure 10B-b, hydrides act as the hydrogen source to promote the formation of the HCOO* intermediate. Next, the $Cu(I)_{25}$ core can dictate subsequent HCOO* binding to give HCOOH. These authors have also explored the possibility of the subsequent reduction of HCOOH to H_2COOH, which is an intermediate to give the CH_3OH and HCHO products. However, this process, either occurred in a proton channel or hydride transfer channel, is very unfavorable, where the Gibbs free energy for H_2COOH formation and energy barrier for subsequent adsorption on Cu surface is calculated to be 1.28–1.32 and 1.40–1.51 eV, respectively (Figure 10B-c). This theoretical study gives further evidence for the electrocatalytic mechanism of CO_2 ERR.

Just recently, Robinson et al. reported $[Cu_{13}(MBO)_{12}H]$ (MBO = 2-mercaptobenzoxazole) (**CuNC-21**).[49] The NC of **CuNC-21** consists of thirteen Cu atoms and twelve MBO ligands, as revealed by single-crystal X-ray analysis. The authors portray the Cu atom in the oxidation state between 0 and +1. As shown in Figure 11A, **CuNC-21** adopts a novel cap–core–cap configuration. In the $Cu_4(MBO)_3$ cap, each MBO ligand binds to a base Cu through an N atom while the S atom links to an adjacent Cu and to the apical Cu. The bonding configuration produces a tilting of the ligand plane relative to the C_3 axis of the Cu_4 pyramid, which imbues chirality on the $Cu_4(MBO)_3$ motif, with either a clockwise or a counter-clockwise arrangement (Figure 11A). The ligands are attached in a twisted fashion relative to the vertical axis, imparting either a clockwise or a counter-clockwise chirality to the $Cu_5(MBO)_6$ core (Figure 11A). For the core, all N atoms are attached to the middle part of the triangular plane of copper atoms, while the S atoms are attached to one apical Cu and also to a basal Cu from an adjacent cap. A hydride located within the Cu_5 core is determined from DFT geometry optimization. The structure of **CuNC-21** involves a tertiary hierarchical complexity assembly. The primary structure shows a combination of the clockwise/counterclockwise core Cu_4 caps and core Cu_5 units. The secondary structure involves the formation of a pair of enantiomeric isomers by cap and core interactions (C—H···π), as shown in Figure 11B. Finally, self-assembly of the alternating enantiomers with hydrogen bonds as the intermolecular driving force has led to a tertiary hierarchical architecture (Figure 11C). It is worth mentioning that an inhomogeneous charge distribution was observed over the Cu_{13} core to bear the Cu(0) character. Fortunately, **CuNC-21** is air-stable for further exploration of its electrocatalytic property. It is active toward CO_2 reduction to produce H_2 (78%), CO (20%) and CH_4 with onset potential at −1.05 V (Figure 11E). Additionally, it is also an active cathode catalyst for oxygen reduction reaction (ORR) to give water and hydrogen peroxide in variable yields, depending on the overpotential applied (Figure 11D). This study points out a new horizon on NC-based hierarchical systems as novel functional materials.

As aforementioned, Cu(I) hydride NCs capable of accumulating hydrides in their structures are expected to act as the hydrogen source, which also offers an opportunity to explore their applications HER. In connection with this, under different conditions including solar irradiation, thermolysis, and acidification, release of H_2 from hydride NCs has become viable, as exemplified by $[Cu(I)_{18}H_{16}(DPPE)_6][BF_4]Cl$ (DPPE = *bis*(diphenylphosphino)ethane), $[Cu(I)_{20}H_{11}\{S_2P(O^iPr)_2\}_9]$, and $[Cu(I)_{28}(H)_{15}(S_2CN^nPr_2)_{12}](PF_6)$ etc.[50] However, these processes were accompanied by the simultaneous degradation of NCs, and hence these CuNCs cannot be taken as robust electrocatalysts. Very remarkably, as aforementioned, by using $[Cu(I)_{32}(H)_{20}\{S_2P(O^iPr)_2\}_{12}]$ (**CuNC-19**) as a catalyst, HER occurs to produce H_2 with a 94% selectivity at an overpotential of 0.6 V.[44] This process involves consumption of the hydrides from the NC via the Heyrovsky mechanism, and subsequent replenishment via the Volmer mechanism from aqueous solution. The high stability of this hydride-rich NC for electrocatalytic applications is remarkable and promising for future development.

3.2 | Chemical sensing

The concentration level of H_2O_2 is an important biological parameter in studying Alzheimer's disease, myocardial infarction, and cancers,[51] which has posed a significant challenge to develop efficient sensors for detection of the H_2O_2 level. In this regard, metal-based electrocatalytic materials have been widely used due to their ability to enhance the electrode conductivity and facilitate the electron transfer. Particularly, the electrocatalytic activity of metal NCs is strongly

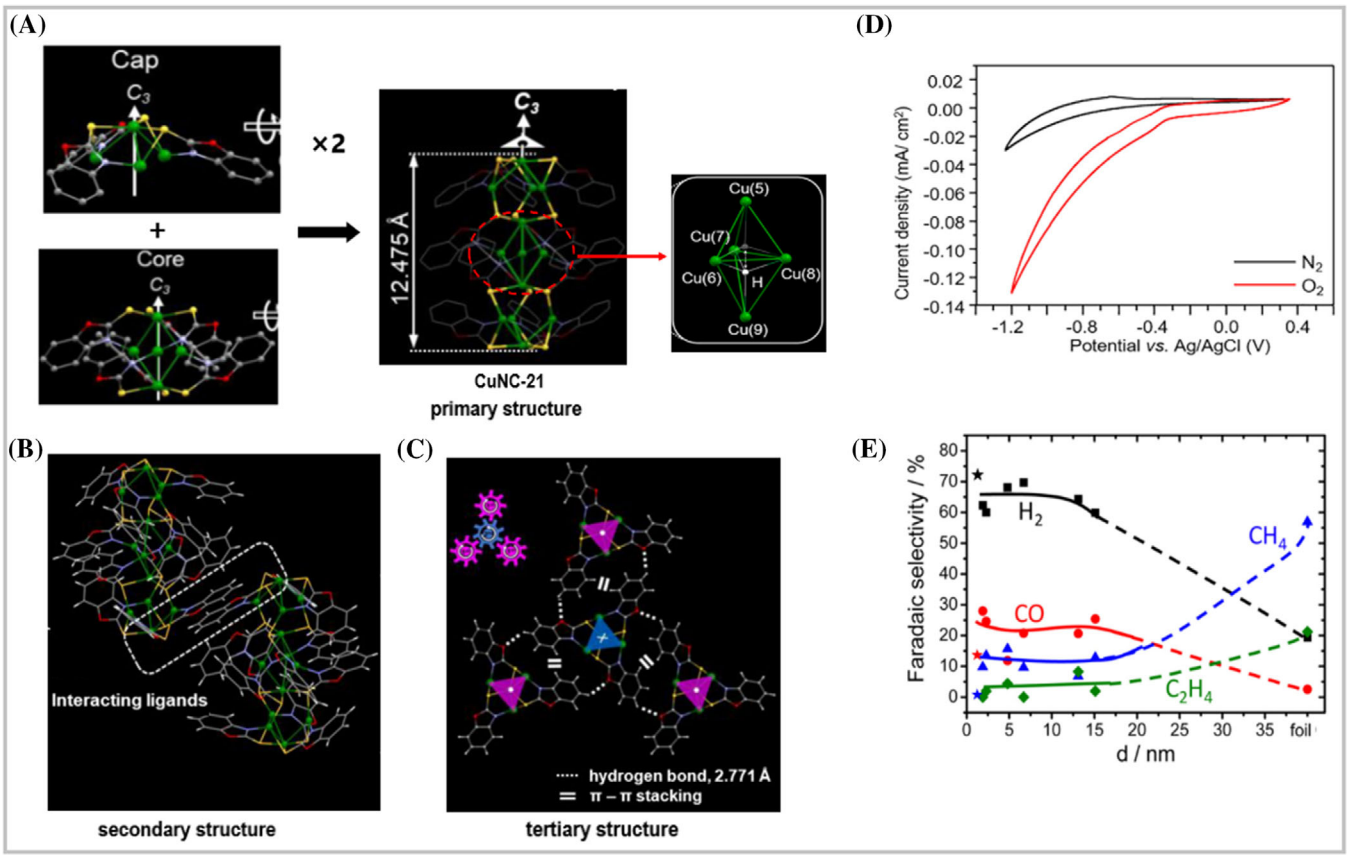

FIGURE 11 (A) Structure of **CuNC-21** as the primary structure. (B) Secondary structure. (C) Tertiary structure. (D) Catalytic activity of **CuNC-21** in ORR and (E) CO_2 ERR. Reproduced with permission.[49] Copyright 2020, American Chemical Society

dependent on the exposed facets, which provides active metal sites for interactions with H_2O_2 to dictate electron transfer to show good electrocatalytic performance.[52] Thus, CuNCs with open metal sites are potential chemical sensors for the detection of H_2O_2.

In 2016, Clayborne and Chen et al. have reported a thiol-protected sub-nanometer cluster $[Cu_6(SC_7H_4NO)_6][Na(C_3H_6O)_6]$ (**CuNC-22**), in which the oxidation state of the Cu atom is between 0 and +1.[53] The Cu_6 core can be viewed as a slightly distorted octahedron (Figure 12A-b). In this Cu_6 cluster, each sulfur atom forms a bond with two Cu atoms. Meanwhile, two S atoms are located at the opposite vertices of an octahedron and four Cu atoms are bonded by a chair-like conformation (Figure 12A-b). Furthermore, the nitrogen atoms form an additional bond with the Cu atoms, thus enhancing their stability and compatibility. **CuNC-22** has a size of about 1.68 nm × 1.45 nm (Figure 12A-a). **CuNC-22** was investigated for electrochemical detection of H_2O_2. The CVs of **CuNC-22**/GC electrode in 0.1 M phosphate buffer solution with different concentrations of H_2O_2 show obvious reduction current after the introduction of H_2O_2 and the reduction current increases with the increase of H_2O_2 concentration (Figure 12A-c). The amperometric *i–t* curve (Figure 12A-d) also suggests that the reduction current increases with the successive addition of H_2O_2 and the current can reach a steady state rapidly, indicating the sensitive and fast response of **CuNC-22** to the concentration change of H_2O_2. The responding current and concentration of H_2O_2 display a linear relationship (Figure 12A-e). The limit of detection (LOD) was estimated to be 1.8×10^{-6} M based on the three times the standard deviation for the average measurement of blank sample (LOD = $3\sigma s^{-1}$). Meanwhile, from the fitting curve, a linear range from 1.8×10^{-6} to 15×10^{-6} M was obtained, which is much wider than some previously reported sensing materials, and both of the LOD and linear range are superior to the previously reported Cu_2O nanomaterials.[54] Furthermore, addition of a variety of analytes shows no influence on the reduction current, also indicative of the high sensitivity of the cluster to H_2O_2 (Figure 12A-f). Even though **CuNC-22** can be considered as a ligand-protected system, the two Cu atoms at the opposing vertices in the octahedron are exposed, which dictates the ability of **CuNC-22** in the electrochemical detection of small molecules. The results provide a new route to use sub-nanoscale Cu clusters as new chemical sensors for H_2O_2.

In 2019, Zang et al. reported a face-centered cubic (fcc) Cu_{14} with Cu(0) character, $[Cu_{14}(C_2B_{10}H_{10}S_2)_6(CH_3CN)_8]$ (**CuNC-23**).[55] As shown in Figure 12B-a, the structure of **CuNC-23** contains a discrete cubic Cu_{14} skeleton with six face-capping bidentate 1,2-dithiolate-*o*-carborane ligands, and eight vertex-capping CH_3CN ligands. Each Cu atom in the Cu_6^{4+} core adopts ten-coordinate geometry, bonding to four adjacent Cu atoms at the octahedral vertices, four Cu atoms from the corresponding face of the cubic Cu_8^{8+} shell, and two S atoms from one 1,2-dithiolate-*o*-carborane ligand. In the Cu_8^{8+} shell, each Cu atom adopts a seven-coordinate geometry, bonding to three S atoms from three different 1,2-dithiolate-*o*-carborane ligands, three Cu atoms of the Cu_6^{4+} unit, and one CH_3CN molecule located at a cubic corner. Each thiolate group links one Cu atom from the Cu_6^{4+} core and two Cu atoms from the Cu_8^{8+} shell.

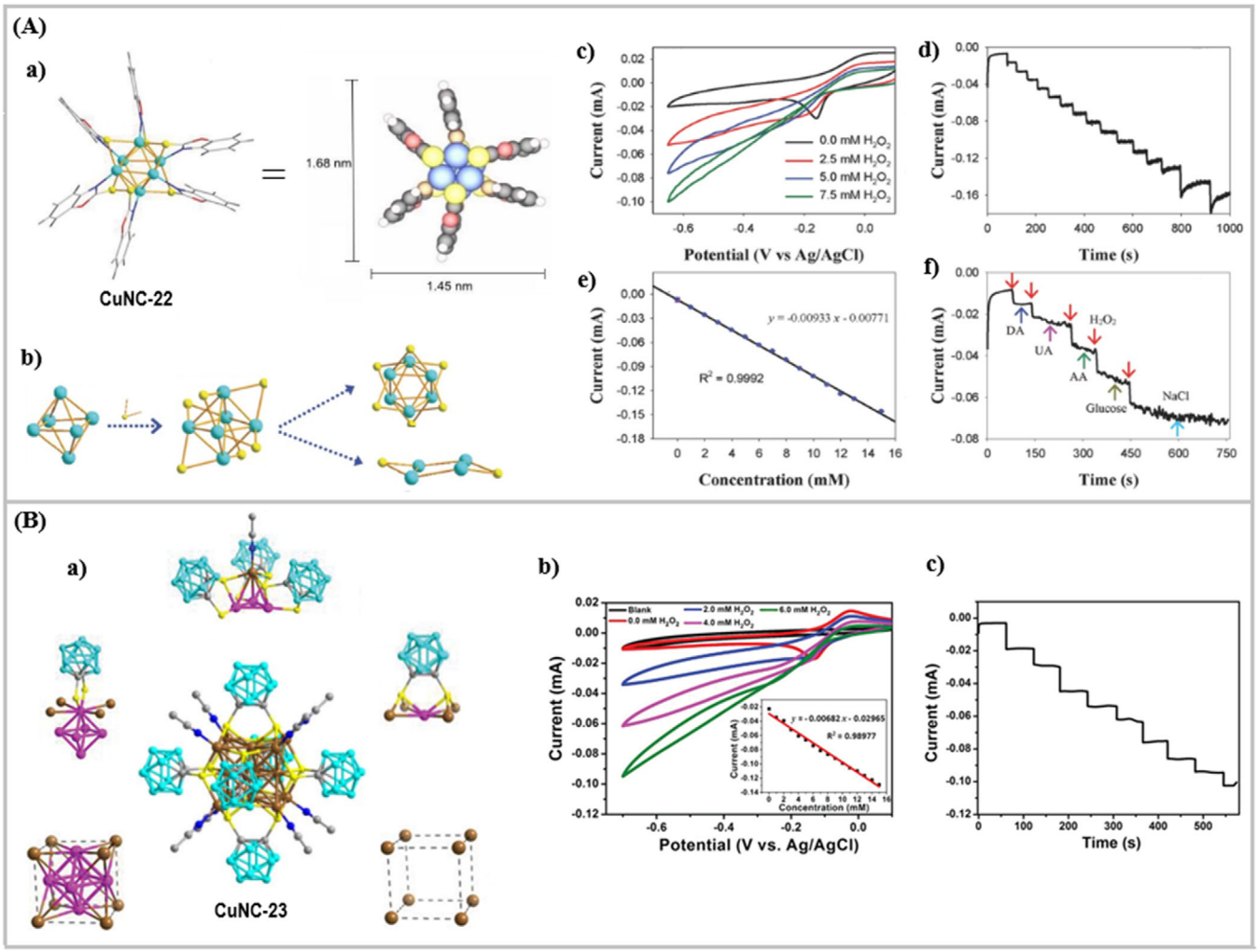

FIGURE 12 A: (a) Structure of **CuNC-22** and (b) its structure anatomy. Color legend: green sphere, Cu; yellow sphere, S; blue sphere, N; red sphere, O; light gray sphere, C; deep gray sphere, H. (c) CVs of the **CuNC-22** with different concentrations of H_2O_2. (d) Amperometric *i*–*t* curve of the **CuNC-22** upon the successive addition of H_2O_2. (e) The linear relationship between the responding current and concentration of H_2O_2. (f) The amperometric responses on alternate addition of interfering chemicals and H_2O_2. Reproduced with permission.[53] Copyright 2016, Wiley. B: (a) Structure anatomy of **CuNC-23**. Color codes: brown and pink = copper; yellow = sulfur; gray = carbon; blue = nitrogen; turquoise = boron. (b) CVs of blank electrode and **CuNC-23** with different concentrations of H_2O_2. (c) Amperometric *i*–*t* curve of **CuNC-23** upon the successive addition of H_2O_2. Reproduced with permission.[55] Copyright 2019, Wiley

In the electrochemical detection experiments of H_2O_2, the CVs of **CuNC-23**/GC electrode show that the reduction current appears after the introduction of H_2O_2 and the reduction current increases with the increasing H_2O_2 concentration (Figure 12B-b). The amperometric *i*–*t* curve of **CuNC-23** to the successive addition of H_2O_2 further demonstrates the sensitive and fast response of **CuNC-23** to the concentration change of H_2O_2 (Figure 12B-c). A linear relationship was also observed between the responding current and concentration of H_2O_2. The LOD was estimated to be 2.3×10^{-6} M based on the standard deviation for the average measurement of the blank sample (LOD = $3\sigma s^{-1}$). It appears that the cavities in **CuNC-23** act as the active sites for the detection of the H_2O_2 molecules.

3.3 | Catalysis in organic synthesis

In pursuit of well-defined nanocatalysts, atomically precise metal NCs are expected to constitute a new class of model catalysts.[56] First, in general, the smaller the size is, the larger the specific surface area would be, and hence the higher the catalytic activity, which can largely enhance the atom-utilization rate of the catalysts. Thus, CuNCs as a unique class of materials that are typically smaller than 3 nm are desirable catalysts. Second, CuNCs show rich compositions and structures and therefore can provide variable active sites for catalyzing a variety of reactions. Third, CuNCs show atomically precise structures that are expected to offer mechanistic insights into the catalytic reactions from both experimental and theoretical viewpoints. As a result, efforts have been devoted to exploring the utilization of CuNCs as catalysts in various types of organic reactions.

Astruc et al. inspected the catalytic property of $[Ph_3PCu(I)H]_6$ and **CuNC-18** in the CuAAC reactions, where the optimized reaction proceeded to give the triazole product with the respective yield of 94% and 99%, which is slightly higher than that of the hydride-free $[Cu_6(C_7H_4NOS)_6]^-$ (Figure 13A).[6] Liu et al. have disclosed a hydride-centered NC of $[Cu(I)_8(\mu_4\text{-}H)\{S_2P(OEt)_2\}_6][PF_6]$ (**CuNC-24**), which can be applied as a catalyst for the cycloaddition of organic azides with both internal and

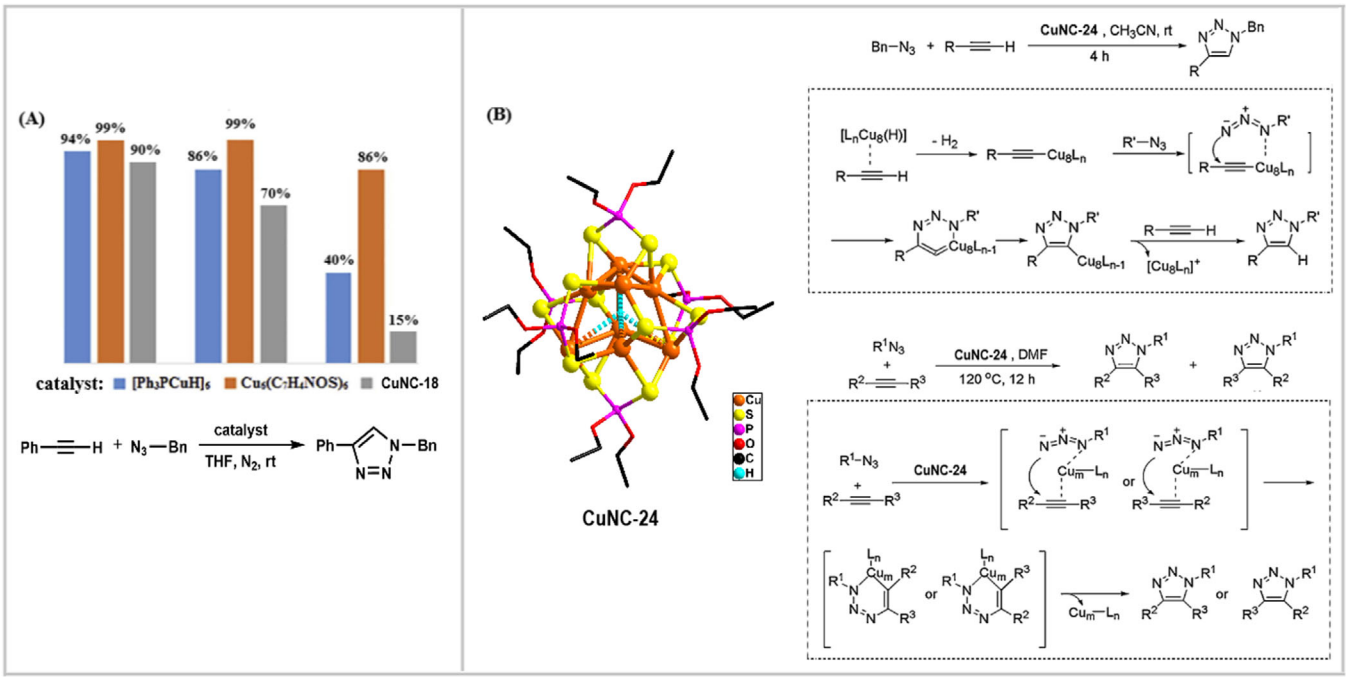

FIGURE 13 (A) Comparison of the catalytic efficiency of three cluster species including **CuNC-18** for CuAAC reactions. Reproduced with permission.[6] Copyright 2018, Wiley. (B) Structure of **CuNC-24** and its catalytic application for the cycloaddition of organic azides with terminal and internal alkynes. Their respective mechanisms are shown in the dotted box. **CuNC-24** is shown in the form of Cu-L complexes to easily illustrate the mechanism. Reproduced with permission.[57] Copyright 2013, Springer Nature

terminal alkynes for preparing the respective substituted triazoles (Figure 13B).[57] With **CuNC-24** loading as low as 0.4 mol%, the reactions of terminal alkynes with BnN_3 proceeded smoothly at ambient temperature to exclusively produce 1,4-triazoles in good yields. It was assumed that the terminal hydrogen of the alkyne was abstracted by the hydrides from the cluster to form the Cu(I) acetylide compound, which is a requisite intermediate for click chemistry. In contrast, **CuNC-24** also exhibits activity in DMF at an elevated temperature for the cycloaddition of internal alkynes to yield 1,4,5-trisubstituted triazoles. Unlike the case of terminal alkynes, it is proposed that the cycloaddition can only be induced after **CuNC-24** simultaneously coordinates with both azides and internal alkynes to give a six-membered metalla-cyclic intermediate. Then, the triazole product is formed accompanied by the release of **CuNC-24** for the next catalytic cycle. Their respective mechanisms have been shown in Figure 13B.

Hayton et al. reported the first example of a two-electron Cu superatom $[Cu_{20}(C{\equiv}CPh)_{12}(OAc)_6]$ (**CuNC-25**).[58] **CuNC-25** contains a tetrahedral $[Cu_4]^{2+}$ core (Figure 14A-a,b), which is encapsulated by the $[Cu_{16}(C{\equiv}CPh)_{12}(OAc)_6]^{2-}$ shell. The twelve acetylide ligands incorporated into the $[Cu_{16}(C{\equiv}CPh)_{12}(OAc)_6]^{2-}$ shell are arranged in four [cyclo-$Cu(C{\equiv}CPh)]_3$ units, which are situated at the vertices of a tetrahedron (Figure 14A-c,d). One of the twelve acetylide ligands adopts a $\mu_4{:}\eta^1,\eta^1,\eta^2,\eta^2$ binding mode, four feature a $\mu_3{:}\eta^1,\eta^1,\eta^2$ binding mode, and seven show a $\mu_4{:}\eta^1,\eta^1,\eta^1,\eta^2$ binding mode. The six acetate ligands are bound in the κ_2 fashion. Whilst a small Cu(I) acetylide cluster bearing the same binding modes of acetylide ligands with **CuNC-25** has been reported to catalyze the [3 + 2] cycloaddition reaction of alkynes and azides,[59] it was found that **CuNC-25** can also catalyze the Huisgen [3 + 2] cycloaddition reaction to give triazoles. In addition, **CuNC-25** can be readily immobilized on dry, partially dehydroxylated silica by the release of 1 equiv of phenylacetylene per NC to give the substituted NC of $[Cu_{20}(C{\equiv}CPh)_{11}(OAc)_6(OSi{\equiv})]$ (**CuNC-25a**, Figure 14A-e), which appears to be a substantially more stable catalyst for the click chemistry reactions under the reaction conditions (Figure 14A-f). More importantly, neither of them requires harsh pretreatment for activation, which suggests the utility of CuNCs as stable catalysts in organometallic synthesis. In terms of the catalytic mechanism, it was proposed that the first step involves reaction of benzyl azide with a bound phenylacetylide ligand, resulting in the formation of a Cu-bound triazolate fragment. This fragment undergoes subsequent protonolysis with an incoming alkyne to generate a triazole product.

Häkkinen and Zheng et al. have reported $[Cu(I)_{25}H_{10}(SPhCl_2)_{18}](PPh_4)_3$ (**CuNC-26**),[60] which is shown in Figure 14B-a. The anatomy of the core structure is based on the different atomic shells. Figure 14B-b shows the $Cu@Cu_{12}$ core as a centered twinned cuboctahedron. Figure 14B-c shows the next layer of metal atoms that forms a truncated v_3 tetrahedral (t3t) shell in such a way that each distorted hexagonal face of the shell aligns with a trigonal face of the cuboctahedron core. Figure 14B-d shows the positions of the S atoms from the thiolate ligands, and DFT-optimized structures with hydrides are also shown in Figure 14B-e. These authors have made use of the hydride components to explore new catalytic reactions, where **CuNC-26** is capable of catalyzing the hydrogenation of ketones to alcohols under mild conditions (Figure 14B-f). Theoretical calculations and experimental results have validated that the hydrogenation reaction only eventuates around the hydride site, and the hydrides are the source for hydrogenation to evoke such single-site mechanism. Specifically, DFT computations have suggested the most plausible pathway, that is, hydrogenation of the ketone by hydrides from the NC leads to the formation

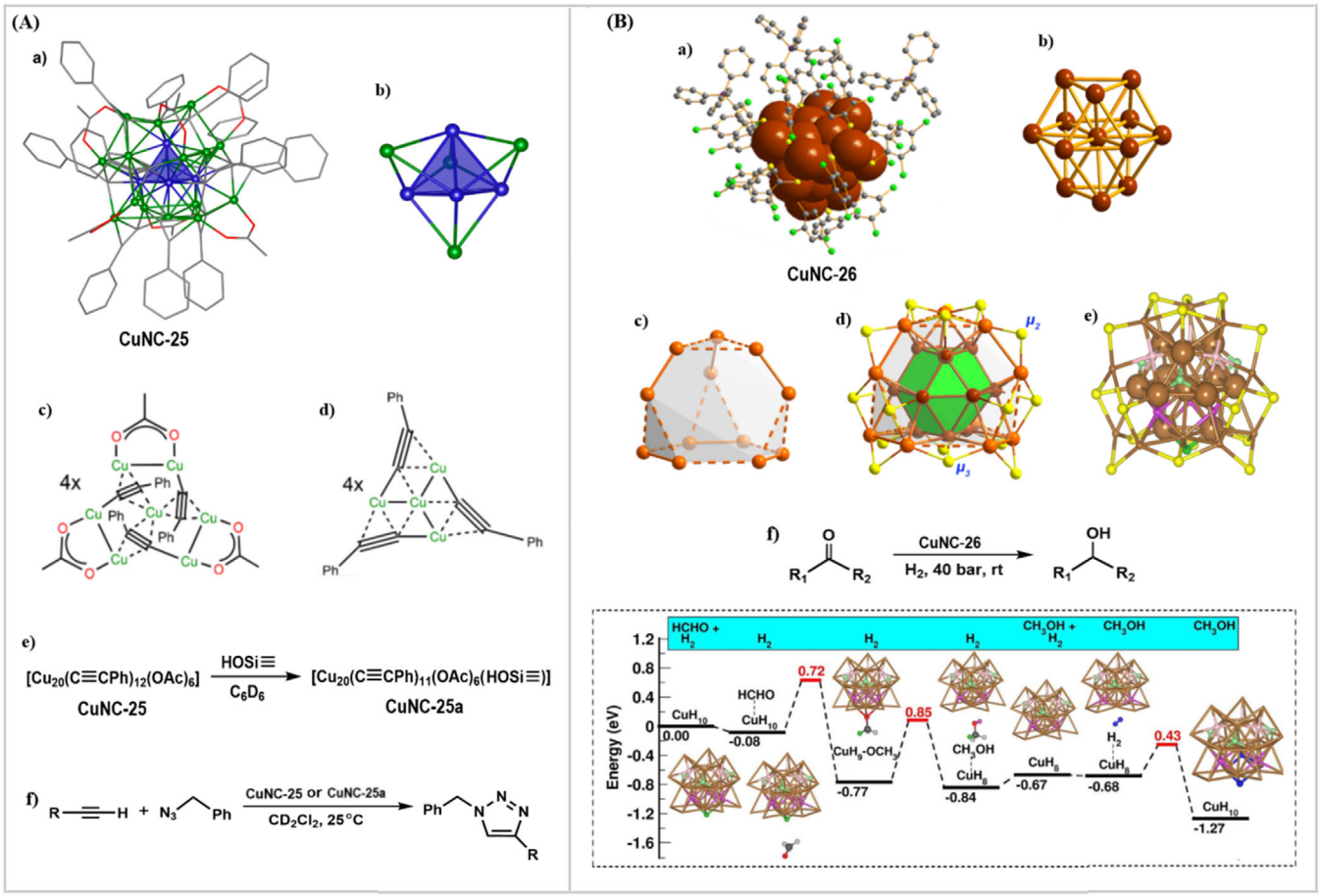

FIGURE 14 A: (a) Structure of **CuNC-25**. (b) Tetrahedral $[Cu_4]^{2+}$ core (blue) along with face-capping Cu atoms (green). Color legend: Cu = blue, green; C = gray; O = red. (c) and (d) Coordination modes of the ligands. (e) Ligand exchange reaction to form **CuNC-25a**. (f) Catalytic application of **CuNC-25** and **CuNC-25a** in [3 + 2] cycloaddition reaction. Reproduced with permission.[58] Copyright 2018, American Chemical Society. B: (a) Structure of **CuNC-26**. Color code: dark-red and light-brown, Cu; gray, C; yellow, S; bright green, Cl; purple, P. (b) Centered twinned cuboctahedron $Cu@Cu_{12}$ inner core. (c) Third layer forming a Cu_{12}-truncated v_3 tetrahedral shell; (d) Cu atoms within the shell and in the two layers bridged by μ_2- and μ_3-S atoms. (e) DFT-optimized structure with the hydrides shown. (f) Catalytic application of **CuNC-26** for thhydrogenation of 2-hexanone and 3-hexanone with the proposed mechanism in the dotted box. In 2-hexanone, R_1 and R_2 are $CH_3(CH_2)_3$— and CH_3—, whereas in 3-hexanone, R_1 and R_2 are $CH_3(CH_2)_2$— and CH_3CH_2—. Reproduced with permission.[60] Copyright 2019, Wiley

of aldehyde and then the alcohol product, wherein the two hydride vacancies in the NC were eventually replenished by H_2. This is the first report to synchronously determine the atomically precise structure and catalytic mechanism of a CuNC for CO_2 ERR.

Tanase et al. have recently utilized a kinetically controlled procedure to synthesize an unsymmetrical NC of $[Cu(I)_8H_6(\mu\text{-dpmppm})_3](PF_6)_2$ (**CuNC-27**, dpmppm = meso-*bis*[(diphenylphosphinomethyl)phenyl phosphino]methane).[61] **CuNC-27** has an unsymmetrical Cu_8 core supported by three dpmppm ligands, in which two apex-shared tetrahedral Cu_4 units (Cu1—Cu4 and Cu4—Cu7) are bridged by Cu8 atom (Figure 15A-a,c). The hydride positions were determined by DFT calculations, where a couple of plausible initial positions were examined by optimization of the hydrides with $\{Cu_8(\mu\text{-dpmppm})_3\}^{8+}$ cluster framework fixed as in the crystal structure, and then all atoms were optimized with B3LYP/Lanl2dz (Cu), 6–311+G** (hydride H), and 6–31G* (others), resulting in the NC structure shown in Figure 15A-b. **CuNC-27** reacted with CO_2 under mild conditions to afford $[Cu(I)_4(\mu\text{-dpmppm})_2\text{-}(HCO_2)_3](PF_6)$ comprising formate bridges. On this basis, catalytic hydrogenation of CO_2 by H_2 to formate in the presence of DBU (1,8-diazabicyclo[5.4.0]undec-7-ene) was established by using **CuNC-27** as a catalyst (Figure 15A-d). The result highlights that the new motif of Cu(I) hydride clusters could be established by the tetraphosphine ligands to boost their reactivity in hydrogenation reactions.

Notably, Tanase et al. also reported $[Cu(I)_8H_6(\mu\text{-dppm})_5](PF_6)_2$ (**CuNC-28**, dppm = *bis*(diphenylphosphino)methane).[62] X-ray analysis establishes the structure of **CuNC-28** to contain an octanuclear Cu(I) cluster consolidated by five dppm ligands (Figure 15B-a). The metal framework is essentially recognized as a *trans*-bicapped octahedron in which the Cu1—Cu6 atoms compose the Cu_6 core and Cu7 and Cu8 atoms cap the octahedron. The $Cu(I)_8$ is protected by dppm ligands to reveal the Cu_8P_{10} overall structure (Figure 15B-c). The six hydride positions were evaluated by DFT optimization (Figure 15B-b). **CuNC-28** shows facile reactivity toward CO_2 that can be developed to give an unprecedented hydrosilylation of CO_2, as shown in Figure 15B-d.

Zhang and his co-workers have synthesized a high-nuclearity CuNC with Cu(0) character, namely, $[Cu_{53}(4\text{-}FC{\equiv}CPh)_9(dppp)_6Cl_6(OAc)_6]$ (**CuNC-29**), where dppp = 1,3-*bis*(diphenylphosphino)propane.[63] The overall structure is shown in Figure 16A-a. Cu atoms are arranged into a five-layer structure protected by four different kinds of

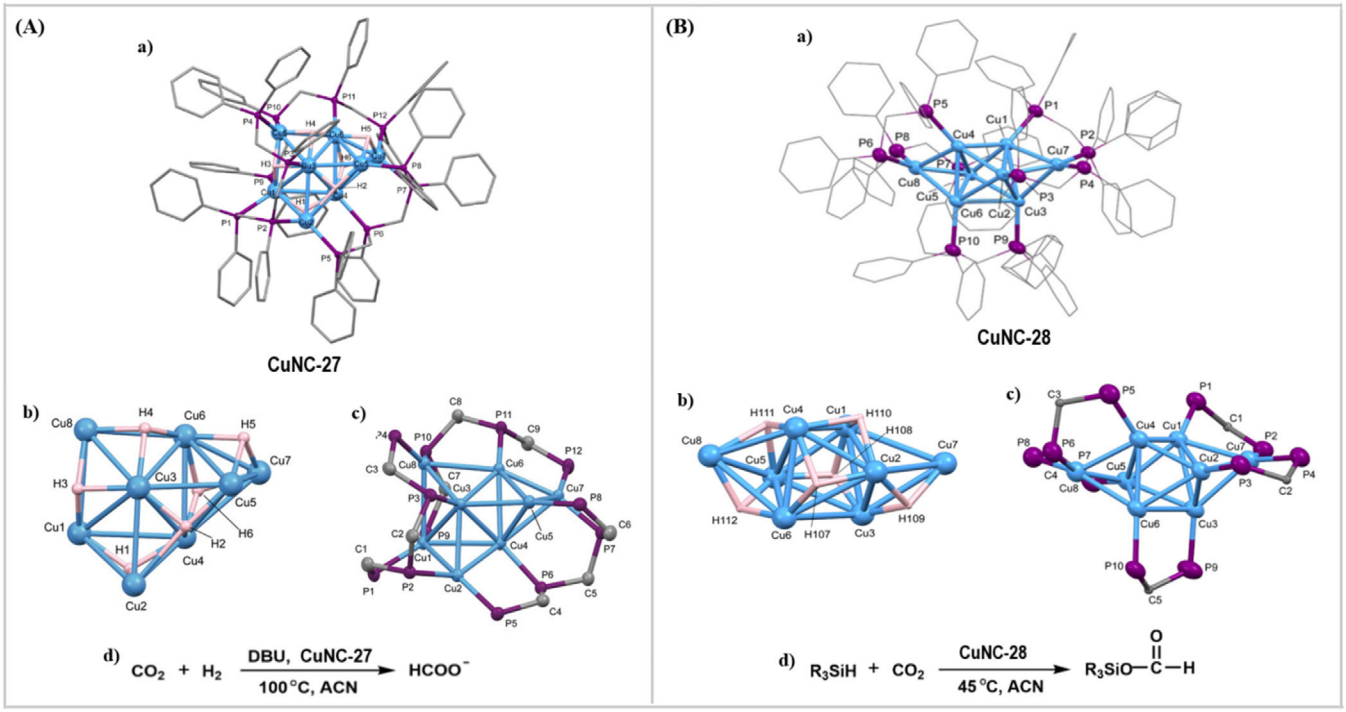

FIGURE 15 A: (a) Structure of **CuNC-27**. (b) $\{Cu_8H_6\}^{2+}$ core structure determined by DFT calculations. (c) Coordination modes of dpmppm with the Cu_8 core. d) Catalytic application of **CuNC-27** for hydrogenation of CO_2. Reproduced with permission.[61] Copyright 2020, Wiley. B: (a) Structure of **CuNC-28**. (b) The $\{Cu_8H_6\}^{2+}$ structure determined by DFT calculations. (c) Coordination modes of dppm with the Cu_8 core. (d) Catalytic application of **CuNC-28** for hydrosilylation of CO_2. Reproduced with permission.[62] Copyright 2017, Wiley

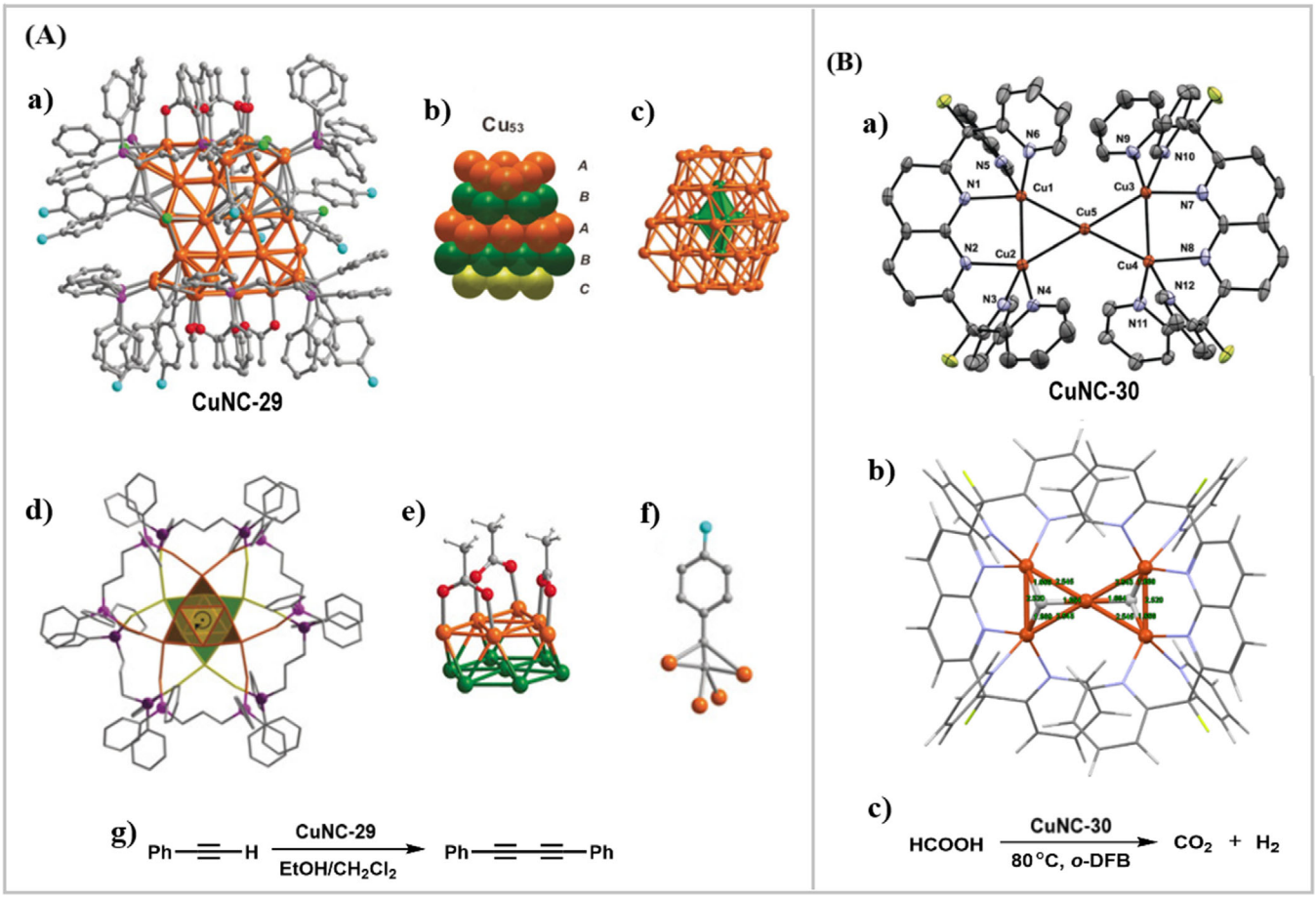

FIGURE 16 A: (a) Structure of **CuNC-29**. Cu orange/green, O red, P purple, Cl green, N dark blue, F light blue, C gray, H white. (b) Layered structure of 41 Cu atoms in Cu_{53}. (c) highlight of five dodeca-coordinated Cu atoms (green color). (d) Top view of the top and bottom layers. (e,f) Coordination modes of acetate groups and 4-fluorophenylacetylene with Cu atoms. (g) Catalytic application of **CuNC-29** for homocoupling of phenylacetylene. Reproduced with permission.[63] Copyright 2020, Wiley. B: (a) Structure of **CuNC-30**. (b) Computed geometry of **CuNC-30** using def2-TZVP to decipher the hydrides. (c) Catalytic application of **CuNC-30** for dehydrogenation of formic acid. Reproduced with permission.[66] Copyright 2020, Wiley

ligands, including nine 4-fluorophenylacetylene, six dppp, six acetate, and six chlorine ligands. Fifty-three Cu atoms fall into two categories, where forty-one of them build up the ABABC layers (Figure 16A-b), and the remaining twelve Cu atoms coordinate with six bidentate dppp ligands. The recently reported NCs with Cu(0) character are characterized by their respective polyhedron kernels with one 12-fold coordinated Cu.[64,65] In **CuNC-29**, there are five such Cu atoms to form a triangular bipyramid (Figure 16A-c). The acetate groups bond with Cu atoms in the μ_2 mode (Figure 16A-e) and each 4-fluorophenylacetylene bonds with four Cu atoms (Figure 16A-f). In Figure 16A-d, a perpendicular view indicates the orientation of the phosphine ligands in a staggered conformation. Experimental results from their catalytic activity in the homocoupling reactions of phenylacetylene are also surprising (Figure 16A-g), where the **CuNC-29** shows the highest activity (substrate conversion of 99.9%). This is probably due to the presence of six small, labile chloride anions, which facilitates the interactions with the substrate to promote the catalytic efficiency.

Tilley group has utilized $[Cu(II)_2(DPFN)(OH)_2](NTf_2)_2$ (DPFN = 2,7-*bis*(fluoro-di(2-pyr-idyl)methyl)-1,8-naphthyridine; NTf = *bis*(trifluoromethanesulfonyl)imide) as a precursor to react with $PhSiH_3$ to synthesize a pentanuclear cluster $[Cu(I)_5(DPFN)_2H_2](NTf_2)_3$ **(CuNC-30)**, in which the $Cu(I)_5$ core adopts a planar "bow tie" configuration (Figure 16B-a,b).[66] In contrast to the putative Cu(I) hydride NCs that are susceptible for CO_2 insertion, this cluster is quite stable under a CO_2 atmosphere. On the contrary, it serves as an efficient catalyst under mild conditions for the dehydrogenation of formic acid to give H_2 and CO_2 (Figure 16B-c). The mechanism of this interesting transformation is unclear. It is very impressive that this Cu(I) hydride cluster exhibits an unusual catalytic reactivity, which may represent useful mimics or models as new Cu(I) hydride catalysts for the dehydrogenation reactions.

Zheng and Heyon et al. have recently prepared $[Cu(I)_{32}(PET)_{24}H_8Cl_2](PPh_4)_2$ (**CuNC-31**, PET = 2-phenylethanethiolate).[67] **CuNC-31** reveals a core–shell structure with a $Cu_{14}H_8$ core and a $Cu_{18}(PET)_{24}Cl_2$ metal-ligand shell. The $Cu_{14}H_8$ unit can be taken as two Cu_8 square antiprisms edge-shared into a rod-shaped Cu_{14} core (Figure 17A). Such a bisquare antiprismatic core is identified for the first time among coinage metal NCs. The metal-ligand shell of the cluster is made up of two simple triangular Cu_2PET and two complex $Cu_7(PET)_{11}Cl$ motifs (Figure 17B). The $Cu_7(PET)_{11}Cl$ motifs appear as a crown, where both Cl are present in the bridging (μ_2) mode (Figure 17C). The triangular Cu_2PET motifs are linked to the $Cu_{14}H_8$ rod on the opposite sides such that two Cu atoms in both motifs are parallel to the edge being shared by the two square antiprisms. Finally, the two $Cu_7(PET)_{11}Cl$ motifs bind to the $Cu_{14}H_8$ core from its left and right side, generating the overall structure of the $Cu_{32}(PET)_{24}H_8Cl_2$ framework (Figure 17D). Electronic calculations have confirmed **CuNC-31** as a zero-free-electron system. Interestingly, it is a highly active homogeneous catalyst toward the C—N bond formation in aniline carbonylation reactions at room temperature to yield carbamates (Figure 17E). Specifically, Cu clusters in $CDCl_3$, aniline, and methyl- and halide-substituted aniline were reacted with diisopropyl azodicarboxylate (DIAD) in an inert atmosphere for 3 h. As a result, the conversion rate of three anilines shows 100%, indicating the high catalytic activity of **CuNC-31**. The isolated yields of the carbamate product for aniline, methyl-substituted aniline, and bromine-substituted aniline are 60.5%, 47.4%, and 46.7%, respectively. Control experiments using CuI and Cu(I)-PET thiolate compound as catalysts only yielded aniline derivatives as the predominate products. The mechanism of aniline carbonylation is believed to proceed via the formation of highly active oxyacyl radicals upon the decomposition of DIAD on Cu catalyst (Figure 17E). The specific interactions between aniline/aniline radicals and the surface of **CuNC-31** would favor the formation of the desired carbamate product. Because such specific interactions are lacking or minimized in the case of CuI or CuPET thiolate, aniline radicals would uncontrollably combine to give a poor selectivity for the carbamate product.

Sun et al. have reported two quasi-structurally isomeric CuNCs of $[Cu(I)_{13}Na_2(CZ\text{-}PrA)_6(TC_4A)_2Cl(MeOH)_2]$ (**CuNC-32a**) and $[Cu(I)_{13}Na(CZ\text{-}PrA)_6(TC_4A)_2(MeOH)]\cdot MeOH\cdot DCM\cdot CH_3COCH_3$ (**CuNC-32b**), where CZ-PrAH = 9-(prop-2-yn-1-yl)-9H-carbazole and H_4TC4A = p-*tert*-butylthiacalix[4]arene, as shown in Figure 18A-a,b.[68] The Cu_{13} kernel is built from a Cu_5 trigonal bipyramid sharing an equatorial Cu atom with a Cu_5 square pyramid, and the other two equatorial Cu atoms each is appended by two more Cu atoms (Figure 18A-c). In contrast, the Cu_5 trigonal bipyramid in **CuNC-32a** is more geometrically deformed due to a bridging Cl^- ion. The CZ-PrA^- ligands show three coordination modes and the $TC4A^{4-}$ ligands show the same coordination mode of μ_4 using both phenolic hydroxyl and bridging sulfur atoms to coordinate with Cu(I) (Figure 18A-d).

In terms of the capability for molecular oxygen activation, **CuNC-32a** exhibits higher $^1O_2$ and lower $O_2^{\bullet-}$ yields than that of **CuNC-32b** (Figure 18B-b,c). This is due to the charge transfer of Cl^- to Cu core ($X_{(Cl)}M_{(Cu)}CT$) in **CuNC-32a** driving blue-shift of the absorption to enlarge the bandgap for easier generation of $^1O_2$ (Figure 18B-a). Correspondingly, **CuNC-32a** and **CuNC-32b** show different photocatalytic properties for the selective oxidation of sulfides. As shown in Figure 18B-d, while the two NCs show the same high conversion rates (>99.9%) of dimethyl sulfide to dimethyl sulfoxide, **CuNC-32a** shows a higher selectivity of 99.9% compared to 93.4% of **CuNC-32b**. Furthermore, the selectivity of **CuNC-32a** for producing methyl phenyl sulfoxide (94.8%) is lower than that for producing dimethyl sulfoxide (99.9%), which indicates the inductive effect of the substituent groups on product selectivity. The reaction mechanism involves $^1O_2$ reacting with sulfide to form a persulfoxide intermediate, followed by oxidation of the persulfoxide intermediate to sulfoxide.

3.4 | Electronic devices

The unique physical and chemical properties of CuNCs make them suitable candidates for various applications. One of the applications is to transform them into electronic devices. As aforementioned, Zhang et al. have reported the application of CuNCs in LED devices.[36] However, the development of CuNC-based devices has only been limited to several examples, and further experimental studies are highly demanded to boost the development of this field.

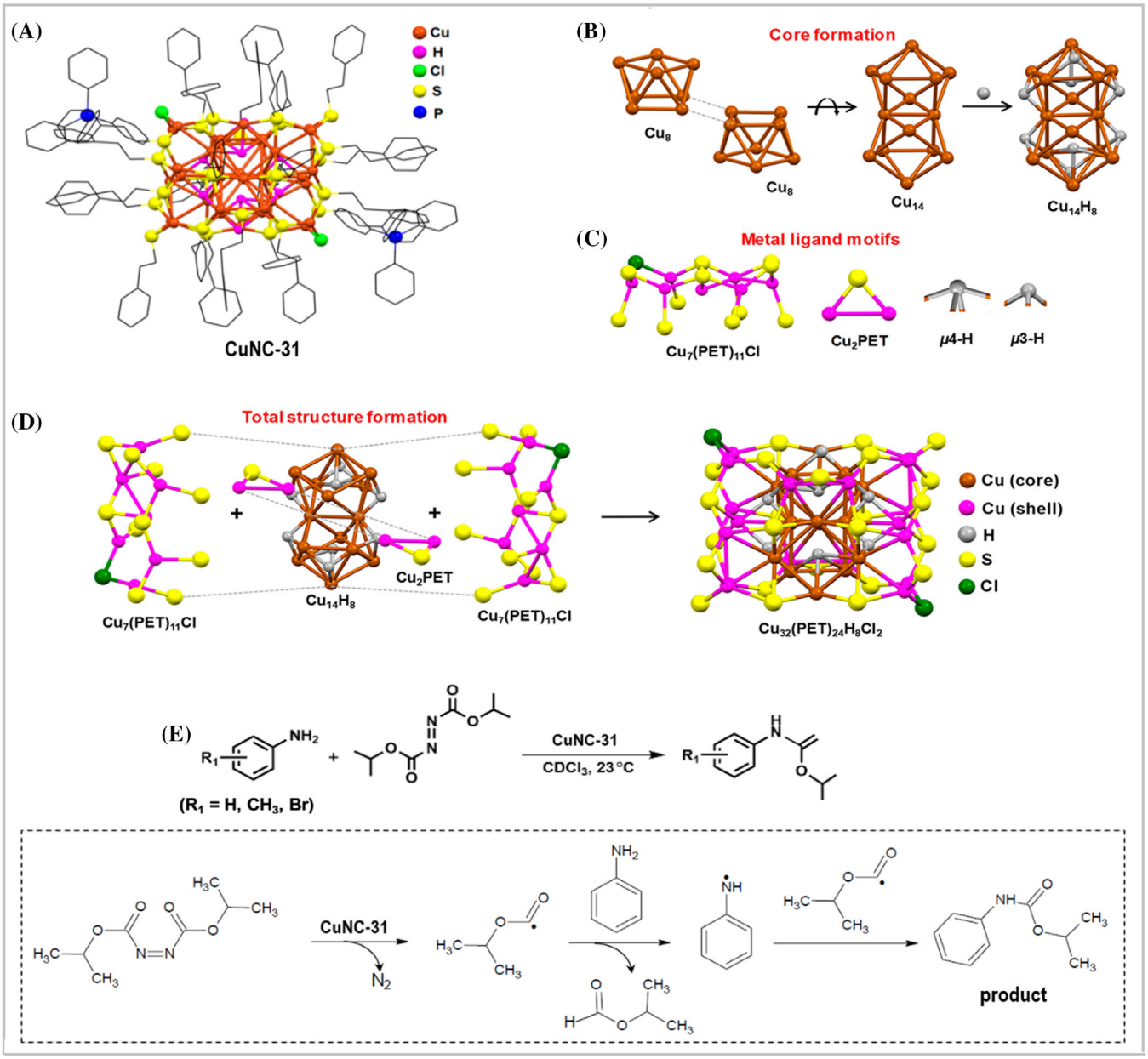

FIGURE 17 (A) Structure of **CuNC-31**. (B) Formation of the $Cu_{14}H_8$ core. (C) Metal-ligand motifs. (D) Linking of motifs with the $Cu_{14}H_8$ core. (E) Catalytic application of **CuNC-31** for the carbonylation of anilines and the proposed mechanism in the dotted box. Reproduced with permission.[67] Copyright 2020, American Chemical Society

Zheng et al. have synthesized a superatomic two-electron NC $[Cu_{53}(CF_3COO)_{10}(C{\equiv}C^tBu)_{20}Cl_2H_{18}]^+$ (**CuNC-33**), the total structure of which is shown in Figure 19A-a. The Cu_{53} skeleton bears a unique four-concentric-shell $Cu_3@Cu_{10}Cl_2@Cu_{20}@Cu_{20}$ structure (Figure 19A-b).[69] Three Cu atoms form an ideal isosceles triangle core. The shell1 is $Cu_{10}Cl_2$, where the twelve atoms are arranged in an icosahedral form with two Cl atoms at the two poles. The shell2 is a Cu_{20} pentagonal dodecahedron. Such an atomic arrangement makes **CuNC-33** the rare case with two concentric icosahedral and dodecahedral shells. The shell3 is a nanowheel with a diameter of 11 Å consisting of twenty Cu atoms (Figure 19A-c). With twenty $^tBuC{\equiv}C^-$, ten CF_3COO^-, and two Cl^- groups ligating on the surface of metal framework, **CuNC-33** has a van der Waals diameter of 1.8 nm. Figure 19A-d illustrates the coordination modes of the various ligands: the twenty $^tBuC{\equiv}C^-$ ligands in two different coordination modes of μ_3-η^1,η^1,η^2, and μ_4-η^1,η^1,η^1,η^2; ten CF_3COO^- as μ_2-η^1,η^1 ligands; as well as two μ_5-chloride ligands. Of comparable interest is that **CuNC-33** is readily soluble in diethyl ether, which allows preparation of a thin film to fabricate an electronic device (Figure 19A-e). By taking this advantage, a device with an FTO/ETL/m-TiO_2/$CH_3NH_3PbI_3$/HTL/Au configuration was adopted. The hole-transport layer (HTL) is the high-quality γ-CuI film, which was converted from the NC by in situ iodination at room temperature. Notably, preparation of high-quality γ-CuI films using conventional wet-chemical methods is very difficult. Upon application, a γ-CuI based perovskite solar cell (PSCs) with 14.3 % of efficiency was achieved. In terms of hysteresis, the device with γ-CuI showed minimal hysteresis, while the device without γ-CuI exhibited severe hysteresis with a relatively low efficiency of 4.0% in the forward scan.

Mak et al. have reported two mixed-valence Cu(I)/Cu(II) NCs, $\{[Cu(II)O_4]{\cdot}[VO_4]_2@Cu(I)_{46}(C{\equiv}C^tBu)_{27}(^tBuPO_3)_2(H_2O)\}{\cdot}(BF_4)_3$ (**CuNC-34**) and $\{[Cu(II)O_6]$

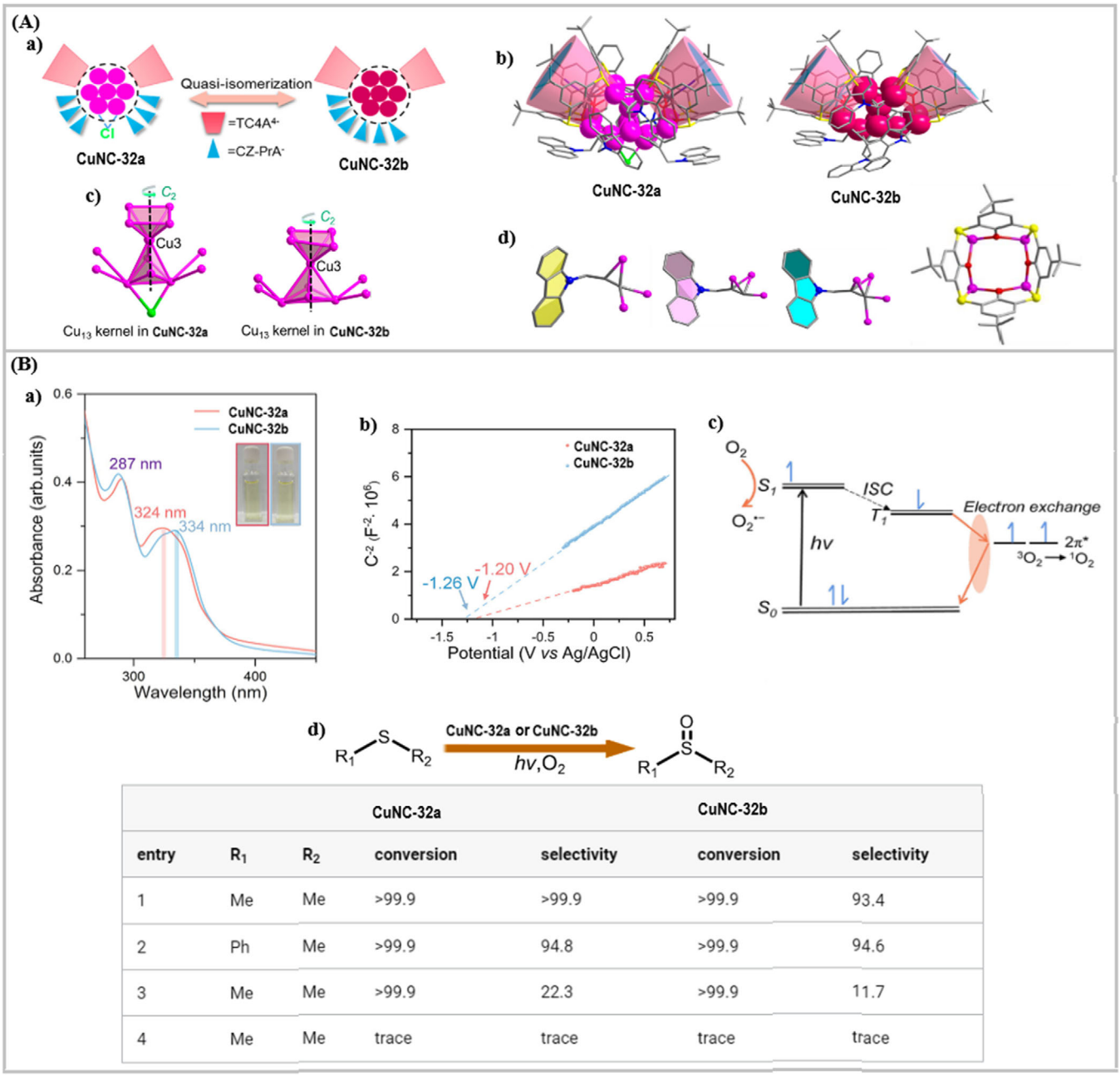

			CuNC-32a		CuNC-32b	
entry	R_1	R_2	conversion	selectivity	conversion	selectivity
1	Me	Me	>99.9	>99.9	>99.9	93.4
2	Ph	Me	>99.9	94.8	>99.9	94.6
3	Me	Me	>99.9	22.3	>99.9	11.7
4	Me	Me	trace	trace	trace	trace

FIGURE 18 A: (a) Illustration of the quasi-isomerization of **CuNC-32a/32b**. (b) Molecular structures of **CuNC-32a/32b**. (c) Cu_{13} kernels. (d) Coordination modes of CZ-PrA$^-$ and TC4A^{4-} ligands. Color labels: purple and red, Cu; cyan, Na; gray, C; red, O; blue, N; yellow, S; green, Cl. B: (a) UV–vis spectra and (b) Mott–Schottky plots. (c) Mechanism of **CuNC-32a/32b** with $^3O_2$ for $^1O_2$ and $O_2^{\bullet-}$ photogeneration. (d) Catalytic application of **CuNC-32a/32b** for the oxidation of sulfides. Reproduced with permission.[68] Copyright 2022, American Chemical Society

@Cu(I)$_{47}$(C≡C^{i}Pr)$_{33}$}·(ClO$_4$)$_4$ (**CuNC-35**). In both NCs, the interstitial Cu(II) cation is stabilized within a Cu(I) shell by forming Cu(I)—O—Cu(II) interactions (Figure 19B-a,b).[26] As shown in Figure 19B-a, the octahedral coordination environment of Cu1 in **CuNC-34** exhibits significant Jahn–Teller distortion, where atoms O1–O4 are equatorial donors with Cu(II)—O bond lengths of 1.940–1.957 Å, and O5 and O6 are axial donors with elongated distances of 2.325 and 2.635 Å, respectively. In **CuNC-35**, Cu1 exhibits a distorted square-planar coordination geometry with Cu(II)—O bond lengths of 1.913(6)–1.945(6) Å (Figure 19B-b). Bond valence sum (BVS) calculations have confirmed the +II oxidation state of the interstitial Cu(II) cation. Furthermore, an electronic device of Cu/sample/Au was fabricated in which the solid pellet of each NC was used as the sample (Figure 19B-c). Based on such device, their activation energies E_a were determined to be around 0.5 eV, and the electrical conductivity is 1.01×10^{-6} S m^{-1} for **CuNC-34** and 1.24×10^{-8} S m^{-1} for **CuNC-35** at the ambient temperature. While the ligand-to-metal charge transfer (LMCT) emission from alkynyl to Cu(I) is quenched by the subsequent intervalence charge transfer (IVCT) from Cu(I) to Cu(II), these successive processes have facilitated the electron transportation to render these two NCs semiconductive. The result suggests the explicit role of the Cu(II) component to lower E_a to give rise to the semiconductive nature.

Sun et al. have reported an air- and moisture-stable NC of [Cu$_{23}$(^{t}BuC≡C)$_{13}$(CF$_3$COO)$_6$] (**CuNC-36**) (Figure 19C-a).[70] **CuNC-36** contains a metallic framework of twenty-three Cu atoms that can be viewed as a [Cu$_4$]^0 tetrahedron

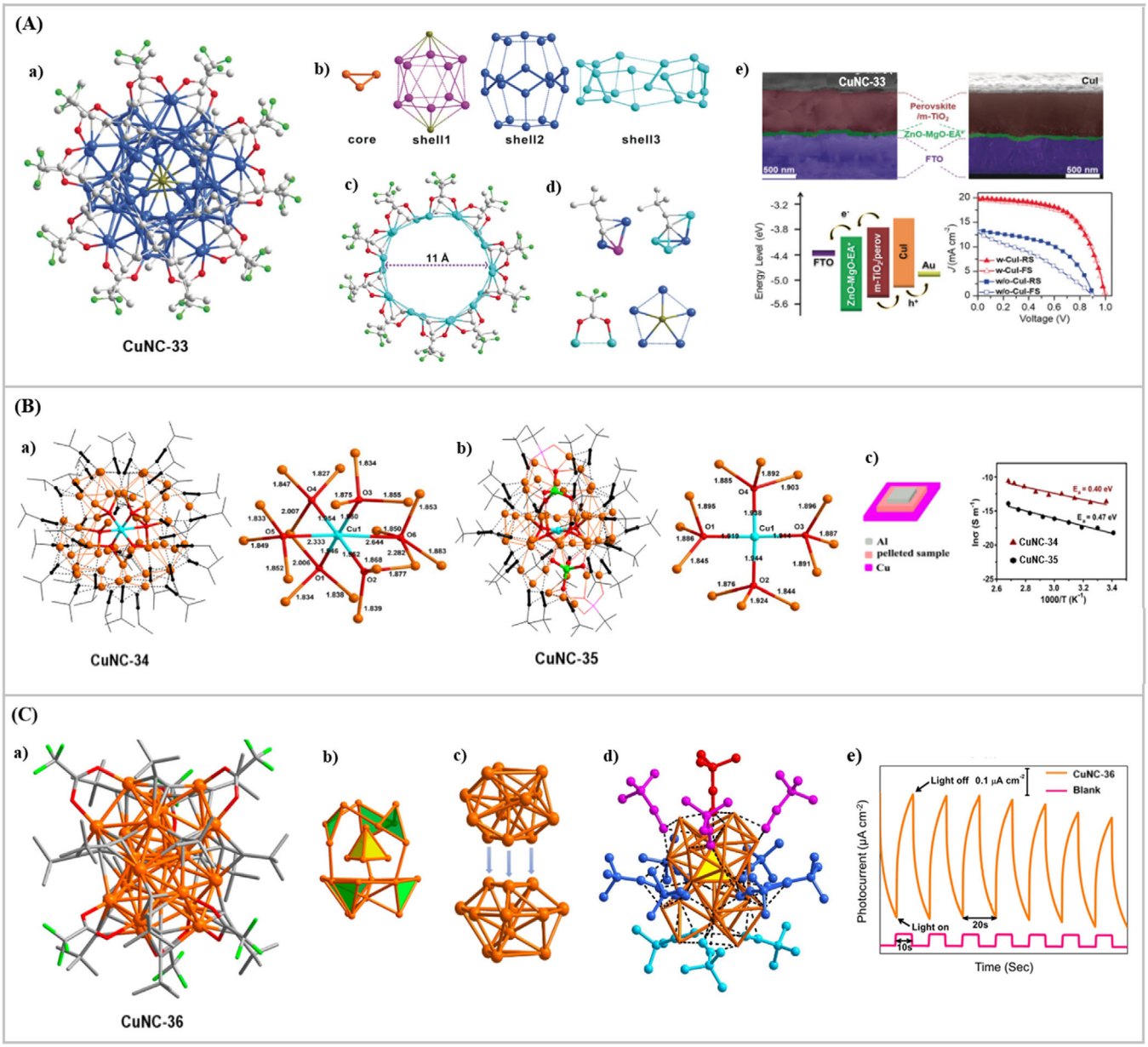

FIGURE 19 A: (a) Structure of **CuNC-33**. Cu in core orange, Cu in shell1 pink, Cu in shell2 blue, Cu in shell3 bluish-green, F light green, Cl dark yellow, O red, C gray. (b) Shell-by-shell representations of the Cu_{53} skeleton, $Cu_3@Cu_{10}Cl_2@Cu_{20}@Cu_{20}$. (c) Structure of shell3. (d) Coordination modes of the ^{t}BuC≡C$^-$, CF_3COO^-, and Cl^- ligands. (e) Electronic device for CuI-based PSC. Reproduced with permission.[69] Copyright 2019, Wiley. B: (a) Structure of **CuNC-34** and (b) **CuNC-35** with the coordination environments of their respective central Cu1 atom shown. (c) Electronic device fabricated to measure their conductivity. Reproduced with permission.[26] Copyright 2019, The Royal Society of Chemistry. C: (a) Structure of **CuNC-36**. (b) Metallic Cu_{23} framework highlighting the central Cu_4 tetrahedron. (c) Anatomy of the Cu_{23} framework as fusion of a distorted icosahedron and cuboctahedron. (d) Coordination modes of the ^{t}BuC≡C$^-$ ligands. (e) Photocurrent curve of **CuNC-36**. Color labels: Orange, Cu; green, F; gray, C; red, O. Reproduced with permission.[70] Copyright 2020, American Chemical Society

surrounded by an outer Cu_{19} shell (Figure 19C-b). Alternatively, it is a severely distorted icosahedron with Cu_4 as a center face-fusing with another severely distorted cuboctahedron (Figure 19C-c). Notably, **CuNC-36** is a rare four-electron superatom with a $1s^21p^2$ electronic shell closure. In addition to the six CF_3COO^- (κ_2-η^1:η^1) ligands, thirteen ^{t}BuC≡C$^-$ ligands consolidate the surface of this architecture by different coordination modes (Figure 19C-d). Due to the broad absorption of this NC in the UV–vis region, the photoelectrochemical properties of **CuNC-36** were explored in a typical three-electrode system using indium tin oxide (ITO) glass as the working electrode, platinum wire as the assisting electrode, and Ag/AgCl as the reference electrode. Practically, **CuNC-36** was spin-coated onto an ITO glass electrode to record the photocurrent. As observed in Figure 19C-e, clear photocurrent responses were observed compared to those of the blank ITO glass. The irradiation light-dependent increase and decrease of photocurrent density indicate that **CuNC-36** exhibits a good generation and separation efficiency of photoinduced electrons/holes pairs in ITO electrodes.

4 | CHALLENGES AND PROSPECTS

The present review describes the current development on atomically precise CuNCs with appealing properties. Despite the fact that progresses have been made in this area, it

remains essentially at an embryonic stage. Particularly in contrast to the fruitful achievements made in AuNCs and AgNCs, significant obstacles have been posed to nourish CuNCs. As shown below, we have suggested some challenges and possible future directions, which are expected to motivate and accelerate the development of this young area.

1. *Synthetic regime*. While the variable oxidation states of Cu have contributed to the structural diversity, this in the meantime makes it thorny to control the accurate synthesis of CuNCs. For example, a library of Au superatoms with magic electron counts from 2-electron to 58-electron systems has been reported. However, only a handful of CuNCs as 2-electron superatoms have been prepared. Thus, a more general methodology to synthesize a particular type of CuNCs is highly desirable. Only when we have an ease of access to CuNCs, we will be able to conduct a more comprehensive analysis on their structure and property characteristics, which in turn offers guidelines for the designed synthesis.
2. *Composition, structure, and size*. Synthetic chemists have been dedicated to assembling NCs larger in size, richer in components, and more complicated in structures. This task challenges our ability to state-of-the-art architectures of CuNCs. In addition to appreciating the elegant NC self-assembly, the rich components and structures are also the origins of new functionalities. Therefore, expanding the scope of CuNCs by introducing new structural elements should be an appealing direction. For instance, polyoxovanadates (POVs) and polyoxtungstates (POWs) are potential candidates to be incorporated. They can either serve as internal templates to be encapsulated within the NCs or exist as large counter anions for NCs. The resulting hybrid nanomaterials are expected to endow with properties inherited from both NCs and POVs/ POWs, which act in synergy for enhanced functionality. However, relevant studies are lacking. In addition, the size effect of metal NCs has been proved to impact the catalytic properties and efficiencies in solar cells. Unfortunately, the situation in CuNCs becomes sticky since we still have no ability to tailor the size of CuNCs.
3. *Photophysical property*. Photophysical property is the central attraction of Cu(I) NCs, and it provides a wide platform for in-depth investigations. Nonetheless, the emission behavior of CuNCs appears to be a case-by-case situation, which owes to their versatile compositions and structures that consequently diversify their emissions. Even for NCs of the same metal nuclearity, distinct packing and arrangement of Cu atoms can lead to different emission properties. Such variable emission property makes the designed synthesis of NCs with functional properties such as TADF and OLEDs a formidable task. Even if theoretical studies can offer some insights into the emission origins, the complicated structures of CuNCs containing hundreds of and even a thousand of atoms have posed limitations to theoretical predictions. Particularly, it is extremely time-consuming and expensive to include all possibilities into calculations to make solid conclusions. So far, we are not aware of any exact rules and working mechanisms on the emission property, not to mention the rational design of specific emissive NCs.
4. *Potential application*. Great promises have been rooted in the appealing properties and prosperous applications of CuNCs. On the one hand, for example, although a number of Cu hydride NCs have been synthesized, only several of them have been subjected to study their activities for CO_2 ERR. Furthermore, by comparison with Cu nanoparticle based electrocatalysts, CuNCs catalysts usually produce CO and HCOOH as products. We are curious to the electrocatalytic activity of the remaining NCs in the generation of other hydrocarbon products. Hence, continuous efforts should be committed to systematically investigating the known properties of CuNCs. On the other hand, the property and application of CuNCs have not been fully discovered. For example, the deep-red NIR emissions with long lifetimes are expected to be utilized in biomedical imaging and sensing. Furthermore, their catalytic activities in organic synthesis can also be expanded to other types of reactions.
5. *Stability*. Simultaneous solubility and stability of CuNCs in solution is a prerequisite for their practical applications. Even in the laboratory research stage, fabrication of electronic devices usually utilizes a solution-processable procedure that requires excellent stability and solubility of materials. However, the Cu-ligand interaction is labile and degradation of high-nuclearity NCs easily occurs in solution, and even if some NCs are stable, their solubility is not good enough to prepare high-quality thin films for fabricating the devices. This problem has largely limited exploration of their applications. In this vein, ligand engineering as a feasible surface functionalization approach may solve this problem. Through careful examination of the peripheral ligands, for example, the choice of bulky and robust ligands, CuNCs are anticipated to show enhanced stability and solubility.
6. *Structure-property correlation*. Materials science addresses the structure and property of materials at a molecular, and hopefully at an atomic level. The most prominent feature of CuNCs is their precise structures and compositions at an atomic precision, and thus CuNCs can serve as benchmark models to elucidate their structure-property correlation. Evidently, this goal is still far from reaching, which is understandable as hinted by the aforementioned points. Although there are limitations and difficulties encountered, it is expected that with the deepening of future research, new aspects of CuNCs can be uncovered, and ultimately the structure-property correlation can be rationalized. In the long run, it is highly desirable to achieve the rational synthesis of well-defined CuNCs to attain desirable properties.

ACKNOWLEDGMENTS

This work was supported by the Science, Technology and Innovation Committee of Shenzhen Municipality (JCYJ20180507183413211), the RGC Senior Research Fellowship Scheme (SRFS2021-5S01), the Hong Kong Research Grants Council (PolyU153062/18P), the Guangdong-Hong Kong-Macao Joint Laboratory of Optoelectronic and Magnetic Functional Materials (2019B121205002), the Hong Kong Polytechnic University (1-ZE1C), Research Institute for Smart Energy (CDAQ), and Miss Clarea Au for the Endowed Professorship in Energy (847S).

CONFLICT OF INTEREST

The authors declare no conflict of interest.

DATA AVAILABILITY STATEMENT

Data sharing is not applicable to this paper as it is a Review paper and no new data were created.

ETHICS STATEMENT

Our paper does not involve human investigation and animal experiments and thus does not need ethics committee approvals.

REFERENCES

1. a) X. Kang, M. Zhu, *Chem. Soc. Rev.* **2019**, *48*, 2422; b) Z. B. Gan, N. Xia, Z. K. Wu, *Acc. Chem. Res.* **2018**, *51*, 2774; c) Q.-M. Wang, Y.-M. Lin, K.-G. Liu, *Acc. Chem. Res.* **2015**, *48*, 1570; d) Q. Li, M. Zhou, W. Y. So, J. C. Huang, M. X. Li, D. R. Kauffman, M. Cotlet, T. Higaki, L. A. Peteanu, Z. Z. Shao, R. Jin, *J. Am. Chem. Soc.* **2019**, *141*, 5314; e) X. Kang, S. X. Wang, Y. B. Song, S. Jin, G. D. Sun, H. Z. Yu, M. Z. Zhu, *Angew. Chem. Int. Ed.* **2016**, *55*, 3611.
2. a) Z. Lei, X.-K. Wan, S.-F. Yuan, Z.-J Guan, Q.-M. Wang, *Acc. Chem. Res.* **2018**, *51*, 2465; b) V. W.-W. Yam, K. K.-W. Lo, *Chem. Soc. Rev.* **1999**, *28*, 323; c) Z.-H. Chen, L.-Y. Zhang, Z.-N. Chen, *Organometallics* **2012**, *31*, 256; d) J.-W. Liu, L. Feng, H.-F. Su, Z. Wang, Q.-Q. Zhao, X.-P. Wang, C.-H. Tung, D. Sun, L.-S. Zheng, *J. Am. Chem. Soc.* **2018**, *140*, 1600; e) Z. Wang, H.-F. Su, C.-H. Tung, D. Sun, L.-S. Zheng, *Nat. Commun.* **2018**, *9*, 4407; f) Z. Wang, H.-F. Su, Y.-Z. Tan, S. Schein, S.-C. Lin, W. Liu, S.-A. Wang, W.-G. Wang, C.-H. Tung, D. Sun, L.-S. Zheng, *Proc. Natl. Acad. Sci. U. S. A.* **2017**, *114*, 12132.
3. a) M. Zhu, C. M. Aikens, F. J. Hollander, G. C. Schatz, R. Jin, *J. Am. Chem. Soc.* **2008**, *130*, 5883; b) W.-H. Fang, L. Zhang, J. Zhang, *J. Am. Chem. Soc.* **2016**, *138*, 7480; c) H. N. Miras, J. Yan, D.-L. Long, L. Cronin, *Chem. Soc. Rev.* **2012**, *41*, 7403; d) Y. Negishi, W. Kurashige, Y. Niihori, K. Nobusada, *Phys. Chem. Chem. Phys.* **2013**, *15*, 18736; e) T. Kawawaki, Y. Kataoka, M. Hirata, Y. Iwamatsu, S. Hossain, Y. Negishi, *Nanoscale Horiz.* **2021**, *6*, 409.
4. a) S. Wang, Y. Song, S. Jin, X. Liu, J. Zhang, Y. Pei, X. Meng, M. Chen, P. Li, M. Zhu, *J. Am. Chem. Soc.* **2015**, *137*, 4018; b) S. Hossain, Y. Niihori, L. V. Nair, B. Kumar, W. Kurashige, Y. Negishi, *Acc. Chem. Res.* **2018**, *51*, 3114; c) G. Soldan, M. A. Aljuhani, M. S. Bootharaju, L. G. AbdulHalim, M. R. Parida, A.-H. Emwas, O. F. Mohammed, O. M. Bakr, *Angew. Chem. Int. Ed.* **2016**, *55*, 5749; d) A. Ghosh, O. F. Mohammed, O. M. Bakr, *Acc. Chem. Res.* **2018**, *51*, 3094; e) Y. Wang, H. Su, L. Ren, S. Malola, S. Lin, B. K. Teo, H. Häkkinen, N. Zheng, *Angew. Chem. Int. Ed.* **2016**, *55*, 15152.
5. a) R. Jin, *Nanoscale* **2015**, *7*, 1549; b) H. Qian, D. Jiang, G. Li, C. Gayathri, A. Das, R. R. Gil, R. Jin, *J. Am. Chem. Soc.* **2012**, *134*, 16159.
6. X. Liu, D. Astruc, *Coord. Chem. Rev.* **2018**, *359*, 112.
7. a) R. C. Maji, P. P. Das, A. Bhandari, S. Mishra, M. Maji, K. B. Ghiassi, M. M. Olmstead, A. K. Patra, *Chem. Commun.* **2017**, *53*, 3334; b) M.-L. Fu, I. Issac, D. Fenske, O. Fuhr, *Angew. Chem. Int. Ed.* **2010**, *49*, 6899; c) D. M. Knotter, A. L. Spek, D. M. Grove, G. van Koten, *Organometallics* **1992**, *11*, 4083; d) C. M. P. Kronenburg, J. T. B. H. Jastrzebski, M. Lutz, A. L. Spek, G. van Koten, *Organometallics* **2003**, *22*, 2312; e) M. D. Janssen, K. Kçhler, M. Herres, A. Dedieu, W. J. J. Smeets, A. L. Spek, D. M. Grove, H. Lang, G. van Koten, *J. Am. Chem. Soc.* **1996**, *118*, 4817.
8. a) T. C. Higgs, P. J. Bailey, S. Parsons, P. A. Tasker, *Angew. Chem. Int. Ed.* **2002**, *41*, 3038; b) X. Y. Chang, K. H. Low, J. Y. Wang, J. S. Huang, C.-M. Che, *Angew. Chem. Int. Ed.* **2016**, *55*, 10312; c) H. Lang, A. Jakob, B. Milde, *Organometallics* **2012**, *31*, 7661; d) R.-W. Huang, J. Yin, C. Dong, A. Ghosh, M. J. Alhilaly, X. Dong, M. N. Hedhili, E. Abou-Hamad, B. Alamer, S. Nematul-loev, Y. Han, O. F. Mohammed, O. M. Bakr, *J. Am. Chem. Soc.* **2020**, *142*, 8696; e) R.-W. Huang, J. Yin, C. Dong, P. Maity, M. N. Hedhili, S. Nematulloev, B. Alamer, A. Ghosh, O. F. Mohammed, O. M. Bakr, *ACS Mater. Lett.* **2021**, *3*, 90.
9. S. K. Barik, S.-C. Huo, C.-Y. Wu, T.-H. Chiu, J.-H. Liao, X. Wang, S. Kahlal, J.-Y. Saillard, C. W. Liu, *Chem. - Eur. J.* **2020**, *26*, 10471.
10. a) R. S. Dhayal, W. E. van Zyl, C. W. Liu, *Acc. Chem. Res.* **2016**, *49*, 86; b) R. S. Dhayal, W. E. van Zyl, C. W. Liu, *Dalton Trans.* **2019**, *48*, 3531.
11. C. Sun, B. K. Teo, C. Deng, J. Lin, G.-G. Luo, C.-H. Tung, D. Sun, *Coord. Chem. Rev.* **2021**, *427*, 213576.
12. T. Nakajima, K. Nakamae, Y. Ura, T. Tanase, *Eur. J. Inorg. Chem.* **2020**, *2020*, 2211.
13. A. Baghdasaryan, T. Bürgi, *Nanoscale* **2021**, *13*, 6283.
14. Y.-E. Shi, J. Ma, A. Feng, Z. Wang, A. L. Rogach, *Aggregate* **2021**, *2*, e112.
15. C.-L. Chan, K.-L. Cheung, W. H. Lam, E. C.-C. Cheng, N.-Y. Zhu, S. W.-K. Choi, V. W.-W. Yam, *Chem. - Asian J.* **2006**, *1*, 273.
16. L.-M. Zhang, T. C. W. Mak, *J. Am. Chem. Soc.* **2016**, *138*, 2909.
17. L. L.-M. Zhang, T. C. W. Mak, *Angew. Chem. Int. Ed.* **2017**, *56*, 16228.
18. S.-S. Zhang, H.-F. Su, G.-L. Zhuang, X.-P. Wang, C.-H. Tung, D. Sun, L.-S. Zheng, *Chem. Commun.* **2018**, *54*, 11905.
19. O. Fuhr, S. Dehnenb, D. Fenske, *Chem. Soc. Rev.* **2013**, *42*, 1871.
20. A. Eichhöfer, G. Buth, S. Lebedkin, M. Kühn, F. Weigend, *Inorg. Chem.* **2015**, *54*, 9413.
21. C. Latouche, J.-H. Liao, Y.-J. Li, R.-Y Shiu, V. Barone, S. Kahlal, C. W. Liu, J.-Y. Saillard, *Inorg. Chem.* **2017**, *56*, 14135.
22. F. Ke, Y. Song, H. Li, C. Zhou, Y. Dua, M. Zhu, *Dalton Trans.* **2019**, *48*, 13921.
23. H. Li, H. Zhai, C. Zhou, Y. Song, F. Ke, W. W. Xu, M. Zhu, *J. Phys. Chem. Lett.* **2020**, *11*, 4891.
24. S. S. Y. Chui, M. F. Y. Ng, C.-M. Che, *Chem. - Eur. J.* **2005**, *11*, 1739.
25. H.-Y. Zhuo, H.-F. Su, Z.-Z. Cao, W. Liu, S.-A. Wang, L. Feng, G.-L. Zhuang, S.-C. Lin, M. Kurmoo, C.-H. Tung, D. Sun, L.-S. Zheng, *Chem. - Eur. J.* **2016**, *22*, 17619.
26. L. L.-M. Zhang, G.-D. Zhou, G. Zhou, H.-K. Lee, N. Zhao, O. V. Prezhdo, T. C. W. Mak, *Chem. Sci.* **2019**, *10*, 10122.
27. J. Luo, Z. Xie, J. W. Y. Lam, L. Cheng, H. Chen, C. Qiu, H. S. Kwok, X. Zhan, Y. Liu, D. Zhu, B. Z. Tang, *Chem. Commun.* **2001**, 1740.
28. a) Z. Wu, Q. Yao, O. J. H. Chai, N. Ding, W. Xu, S. Zang, J. Xie, *Angew. Chem. Int. Ed.* **2020**, *59*, 9934; b) N. Goswami, Q. Yao, Z. Luo, J. Li, T. Chen, J. Xie, *J. Phys. Chem. Lett.* **2016**, *7*, 962; c) Y. G. Srinivasulu, N. Goswami, Q. Yao, J. Xie, *J. Phys. Chem. C* **2021**, *125*, 4066; d) D. Bain, S. Maity, A. Patra, *Chem. Commun.* **2020**, *56*, 9292; e) Z. Wang, Z. Zhu, C. Zhao, Q. Yao, X. Li, H. Liu, F. Du, X. Yuan, J. Xie, *Chem. - Asian J.* **2019**, *14*, 765; f) D. Bera, N. Goswami, *J. Phys. Chem. Lett.* **2021**, *12*, 9033.
29. J. Kumar, T. Nakashima, T. Kawai, *J. Phys. Chem. Lett.* **2015**, *6*, 3445.
30. C. Zhang, S. Li, X.-Y. Dong, S.-Q. Zang, *Aggregate* **2021**, *2*, e48.
31. M.-M. Zhang, X.-Y. Dong, Z.-Y. Wang, H.-Y. Li, S.-J. Li, X. Zhao, S.-Q. Zang, *Angew. Chem. Int. Ed.* **2020**, *59*, 10052.
32. Y. Jin, S. Li, Z. Han, B.-J. Yan, H.-Y. Li, X.-Y. Dong, S.-Q. Zang, *Angew. Chem. Int. Ed.* **2019**, *58*, 12143.
33. Y.-J. Kong, Z.-P. Yan, S. Li, H.-F. Su, K. Li, Y.-X. Zheng, S.-Q. Zang, *Angew. Chem. Int. Ed.* **2020**, *59*, 5336.
34. S. Nematulloev, R.-W. Huang, J. Yin, A. Shkurenko, C. Dong, A. Ghosh, B. Alamer, R. Naphade, M. N. Hedhili, P. Maity, M. Eddaoudi, O. F. Mohammed, O. M. Bakr, *Small* **2021**, *17*, 2006839.
35. P.-P. Sun, B.-L. Han, H.-G. Li, C.-K. Zhang, X. Xin, J.-M. Dou, Z.-Y. Gao, D. Sun, *Angew. Chem. Int. Ed.* **2022**, *61*, e202200180.
36. Z. Wu, J. Liu, Y. Gao, H. Liu, T. Li, H. Zou, Z. Wang, K. Zhang, Y. Wang, H. Zhang, B. Yang, *J. Am. Chem. Soc.* **2015**, *137*, 12906.
37. Z. Wu, H. Liu, T. Li, J. Liu, J. Yin, O. F. Mohammed, O. M. Bakr, Y. Liu, B. Yang, H. Zhang, *J. Am. Chem. Soc.* **2017**, *139*, 4318.
38. X. Tan, C. Yu, Y. Ren, S. Cui, W. Li, J. Qiu, *Energy Environ. Sci.* **2021**, *14*, 765.
39. D. Wakerley, S. Lamaison, F. Ozanam, N. Menguy, D. Mercier, P. Marcus, M. Fontecave, V. Mougel, *Nat. Mater.* **2019**, *18*, 1222.
40. L. Zhang, X.-X. Li, Z.-L. Lang, Y. Liu, J. Liu, L. Yuan, W.-Y. Lu, Y.-S. Xia, L.-Z. Dong, D.-Q. Yuan, Y.-Q. Lan, *J. Am. Chem. Soc.* **2021**, *143*, 3808.
41. R. S. Dhayal, J.-H. Liao, X. Wang, Y.-C. Liu, M.-H. Chiang, S. Kahlal, J.-Y. Saillard, C. W. Liu, *Angew. Chem. Int. Ed.* **2015**, *54*, 13604.
42. S. Wang, Z. Wu, S. Dai, D.-E. Jiang, *Angew. Chem. Int. Ed.* **2021**, *60*, 12289.
43. T.-A. D. Nguyen, B. R. Goldsmith, H. T. Zaman, G. Wu, B. Peters, T. W. Hayton, *Chem. - Eur. J.* **2015**, *21*, 5341.
44. a) Q. Tang, Y. Lee, D.-Y. Li, W. Choi, C. W. Liu, D. Lee, D-E Jiang, *J. Am. Chem. Soc.* **2017**, *139*, 9728; b) R. S. Dhayal, J. H. Liao, S. Kahlal,

X. Wang, Y. C. Liu, M. H. Chiang, W. E. van Zyl, J. Y. Saillard, C. W. Liu, *Chem. - Eur. J.* **2015**, *21*, 8369.
45. C. W. Li, M. W. Kanan, *J. Am. Chem. Soc.* **2012**, *134*, 7231.
46. Y. Hori, A. Murata, R. Takahashi, *J. Chem. Soc., Faraday Trans.* **1989**, *85*, 2309.
47. T. A. Nguyen, Z. R. Jones, B. R. Goldsmith, W. R. Buratto, G. Wu, S. L. Scott, T. W. Hayton, *J. Am. Chem. Soc.* **2015**, *137*, 13319.
48. F. Li, Q. Tang, *J. Catal.* **2020**, *387*, 95.
49. H. Han, Y. Yao, A. Bhargava, Z. Wei, Z. Tang, J. Suntivich, O. Voznyy, R. D. Robinson, *J. Am. Chem. Soc.* **2020**, *142*, 14495.
50. a) J. Li, H. Z. Ma, G. E. Reid, A. J. Edwards, Y. Hong, J. M. White, R. J. Mulder, R. A. J. O'Hair, *Chem. - Eur. J.* **2018**, *24*, 2070; b) A. J. Edwards, R. S. Dhayal, P.-K. Liao, J.-H. Liao, M.-H. Chiang, R. O. Piltz, S. Kahlal, J.-Y. Saillard, C. W. Liu, *Angew. Chem. Int. Ed.* **2014**, *53*, 7214; c) R. S. Dhayal, J.-H. Liao, X. Wang, Y.-C. Liu, M.-H. Chiang, S. Kahlal, J.-Y. Saillard, C. W. Liu, *Angew. Chem. Int. Ed.* **2015**, *54*, 13604.
51. J. Ju, W. Chen, *Anal. Chem.* **2015**, *87*, 1903.
52. M. Li, D.-P. Yang, X. Wang, J. Lu, D. Cui, *Nanoscale Res. Lett.* **2013**, *8*, 182.
53. X. Gao, S. He, C. Zhang, C. Du, X. Chen, W. Xing, S. Chen, A. Clayborne, W. Chen, *Adv. Sci.* **2016**, *3*, 1600126.
54. M. M. Liu, R. Liu, W. Chen, *Biosens. Bioelectron.* **2013**, *45*, 206.
55. Y.-L. Li, J. Wang, P. Luo, X.-H. Ma, X.-Y. Dong, Z.-Y. Wang, C.-X. Du, S.-Q. Zang, T. C. W. Mak, *Adv. Sci.* **2019**, *6*, 1900833.
56. J. Fang, B. Zhang, Q. Yao, Y. Yang, J. Xie, N. Yan, *Coord. Chem. Rev.* **2016**, *322*, 1.
57. B. H. Lee, C. C. Wu, X. Fang, C. W. Liu, J. L. Zhu, *Catal. Lett.* **2013**, *143*, 572.
58. A. W. Cook, Z. R. Jones, G. Wu, S. L. Scott, T. W. Hayton, *J. Am. Chem. Soc.* **2018**, *140*, 394.
59. A. Makarem, R. Berg, F. Rominger, B. F. Straub, *Angew. Chem. Int. Ed.* **2015**, *54*, 7431.
60. C. Sun, N. Mammen, S. Kaappa, P. Yuan, G. Deng, C. Zhao, J. Yan, S. Malola, K. Honkala, H. Häkkinen, B. K. Teo, N. Zheng, *ACS Nano* **2019**, *13*, 5975.
61. K. Nakamae, T. Nakajima, Y. Ura, Y. Kitagawa, T. Tanase, *Angew. Chem. Int. Ed.* **2020**, *59*, 2262.
62. K. Nakamae, M. Tanaka, B. Kure, T. Nakajima, Y. Ura, T. Tanase, *Chem. - Eur. J.* **2017**, *23*, 9457.
63. M. Qu, F.-Q. Zhang, D.-H. Wang, H. Li, J.-J. Hou, X.-M. Zhang, *Angew. Chem. Int. Ed.* **2020**, *59*, 6507.
64. K. K. Chakrahari, J. H. Liao, S. Kahlal, Y. C. Liu, M. H. Chiang, J. Y. Saillard, C. W. Liu, *Angew. Chem. Int. Ed.* **2016**, *55*, 14704.
65. R. P. B. Silalahi, K. K. Chakrahari, J.-H. Liao, S. Kahlal, Y.-C. Liu, M.-H. Chiang, J.-Y. Saillard, C. W. Liu, *Chem. - Asian J.* **2018**, *13*, 500.
66. A. N. Desnoyer, A. Nicolay, M. S. Ziegler, N. A. Torquato, T. D. Tilley, *Angew. Chem. Int. Ed.* **2020**, *59*, 12769.
67. S. Lee, M. S. Bootharaju, G. Deng, S. Malola, W. Baek, H. H. kkinen, N. Zheng, T. Hyeon, *J. Am. Chem. Soc.* **2020**, *142*, 13974.
68. C. Zhang, Z. Wang, W.-D. Si, L. Wang, J.-M. Dou, Z.-Y. Gao, C.-H. Tung, D. Sun, *ACS Nano* **2022**, *16*, 9598.
69. P. Yuan, R. H. Chen, X. M. Zhang, F. J. Chen, J. Z. Yan, C. F. Sun, D. H. Ou, J. Peng, S. C. Lin, Z. C. Tang, B. K. Teo, L. S. Zheng, N. F. Zheng, *Angew. Chem. Int. Ed.* **2019**, *58*, 835.
70. B.-L. Han, Z. Liu, L. Feng, Z. Wang, R. K. Gupta, C. M. Aikens, C.-H. Tung, D. Sun, *J. Am. Chem. Soc.* **2020**, *142*, 5834.

AUTHOR BIOGRAPHIES

Li-Min Zhang received his Ph.D. degree from The Chinese University of Hong Kong in 2017. He is currently an Assistant Professor in the Department of Applied Biology and Chemical Technology at The Hong Kong Polytechnic University. His research interest focuses on the synthesis, structure, and property of atomically precise metal nanoclusters.

Wai-Yeung Wong received his Ph.D. degree from The University of Hong Kong in 1995. He is currently Chair Professor of Chemical Technology, Clarea Au Professor in Energy, and Dean of the Faculty of Science at The Hong Kong Polytechnic University. He is the President of the Hong Kong Chemical Society. He is also the recipient of the RSC Chemistry of the Transition Metals Award from the United Kingdom, State Natural Science Award (second-class) from China, Croucher Senior Research Fellowship, and RGC Senior Research Fellow Award from Hong Kong. His research interest focuses on the design, synthesis, and application of metallopolymers, metallophosphors, and metal-based nanomaterials.

How to cite this article: L. L.-M. Zhang, W.-Y. Wong, *Aggregate* **2023**, *4,* e266.
https://doi.org/10.1002/agt2.266